

Advanced characterization methods of carrier transport in quantum dot photovoltaic solar cells



Cite as: J. Appl. Phys. 129, 091101 (2021); doi: 10.1063/5.0029440

Submitted: 16 September 2020 · Accepted: 31 December 2020 ·

Published Online: 2 March 2021



View Online



Export Citation



CrossMark

Lilei Hu^{a)} and Andreas Mandelis^{b)} 

AFFILIATIONS

Center for Advanced Diffusion-Wave and Photoacoustic Technologies, MIE, University of Toronto, 5 King's College Road, Toronto, Ontario M5S 3G8, Canada

^{a)}**Present address:** School of Microelectronics, Shanghai University, Shanghai 200444, China.

^{b)}**Author to whom correspondence should be addressed:** mandelis@mie.utoronto.ca

ABSTRACT

Solution-processed colloidal quantum dot (CQD) solar cells are lightweight, flexible, inexpensive, and can be spray-coated on various substrates. However, their power conversion efficiency is still insufficient for commercial applications. To further boost CQD solar cell efficiency, researchers need to better understand and control how charge carriers and excitons transport in CQD thin films, i.e., the CQD solar cell electrical parameters including carrier lifetime, diffusion length, diffusivity, mobility, drift length, trap state density, and doping density. These parameters play key roles in determining CQD thin film thickness and surface passivation ligands in CQD solar cell fabrication processes. To characterize these CQD solar cell parameters, researchers have mostly used transient techniques, such as short-circuit current/open-circuit voltage decay, photoconductance decay, and time-resolved photoluminescence. These transient techniques based on the time-dependent excess carrier density decay generally exhibit an exponential profile, but they differ in the signal collection physics and can only be used in some particular scenarios. Furthermore, photovoltaic characterization techniques are moving from contact to non-contact, from steady-state to dynamic, and from small-spot testing to large-area imaging; what are the challenges, limitations, and prospects? To answer these questions, this Tutorial, in the context of CQD thin film and solar cell characterization, looks at trends in characterization technique development by comparing various conventional techniques in meeting research and/or industrial demands. For a good physical understanding of material properties, the basic physics of CQD materials and devices are reviewed first, followed by a detailed discussion of various characterization techniques and their suitability for CQD photovoltaic devices.

Published under license by AIP Publishing. <https://doi.org/10.1063/5.0029440>

I. INTRODUCTION TO QUANTUM DOTS AND COLLOIDAL QUANTUM DOT SOLAR CELLS

Due to the confined particle motion in three spatial dimensions, the unique optical and electrical properties of quantum dots (QDs) make them promising candidates for fabricating low-cost, large-area, lightweight, flexible, high-efficiency photovoltaic solar cells. These QDs can be made from semiconductor materials, including PbS, PbSe, CdTe, AgBr, InP, InZnP, InAs/CdSe/CdS, and many others, and currently, the highest efficiency for QD-based solar cells is 16.6%.¹ Therefore, this section will introduce QDs and colloidal quantum dot (CQD) solar cells from solution-based CQD fabrication methodologies to discussing the effects of ligand-determined interdot distance, temperature, spatial and energy

disorders, dot size, and dot size polydispersities on QD electrical properties. Last, a discussion of CQD solar cells in this tutorial is focused on their fundamentals, classification, working principles, and efficiency-limiting factors.

A. Synthesis of quantum dots

1. Solution-processed quantum dot synthesis

Two main approaches have been developed for synthesizing QDs in the latest several decades: (1) solution-processed colloidal chemistry methods and (2) lithographic growth which includes the subsequent processing techniques such as various deposition and etching methodologies. The colloidal chemistry fabrication starts

with the rapid injection of semiconductor precursors into a hot and vigorously stirred organic solvent, which contains organic molecules with long chains and can coordinate with the precipitated CQD particles on the surface. Through proper surface engineering using various ligands, these water-soluble CQDs are suitable for various optoelectronic and photovoltaic applications. In comparison, the lithographic growth of QDs is more time-consuming and expensive. Moreover, QDs fabricated through this technique are more easily contaminated during the fabrication process. Contamination can introduce various material defect states, a high degree of dot size polydispersity, and poor interface quality.

There are two types of QD epitaxial growth techniques: vapor phase epitaxy (VPE) and liquid phase epitaxy (LPE). For example, InAs QDs have been fabricated using vapor phase epitaxy for $1.55\text{ }\mu\text{m}$ optical device applications² and growth of self-assembled PbSe quantum dots on GaSb by LPE.³ LPE is commonly used for fabricating semiconductor materials on the micro-scale but infrequently used in QD fabrications. Metalorganic vapor phase epitaxy (MOVPE) using a metalorganic medium and molecular beam epitaxy (MBE) through the Stranski-Krastanov growth mode are the two main techniques that have been widely used for QD synthesis. For example, MBE has been widely implemented in investigating single-photon sources and quantum computation. As reviewed in Ref. 4, III-V semiconductors such as InAs and InGaAs QD have been studied extensively. Although epitaxial growth can

produce QDs with relatively higher quality, when compared with lithographic growth it is uncommonly used for large-scale QD fabrication. Concerning QD quality and size polydispersity, QD synthesis through the pyrolysis of metalorganic precursors is the most successful nanoparticle preparation method. A detailed review of such techniques has been reported by Wang *et al.*⁵ As shown in Fig. 1, the QD preparation mechanism generally can be understood through La Mer and Dinegar's model in the way that precursor nucleation occurs through the rapid injection of QD precursors into a coordinating organic solvent.⁶ In the organic solvent, semiconductor precursors thermally decompose into monomers at a temperature ranging from $120\text{ }^{\circ}\text{C}$ to $360\text{ }^{\circ}\text{C}$, a process to increase the monomer concentration in the solvent. When the monomer concentration surpasses the nucleation threshold concentration, nucleation processes begin and nanoparticles grow quickly through absorbing monomers from the solution-phase. New nuclei can no longer be formed once the monomer concentration is smaller than the critical nucleation threshold concentration, which keeps a constant population of CQDs while the dot size continues to grow through absorbing more monomers in the solution. This process will continue until the monomers are depleted. Due to the depletion of monomers in the solution, the CQD growth process evolves to the Ostwald stage, where smaller CQDs dissolve into monomers because of their higher surface energy. The dissolved monomers contribute

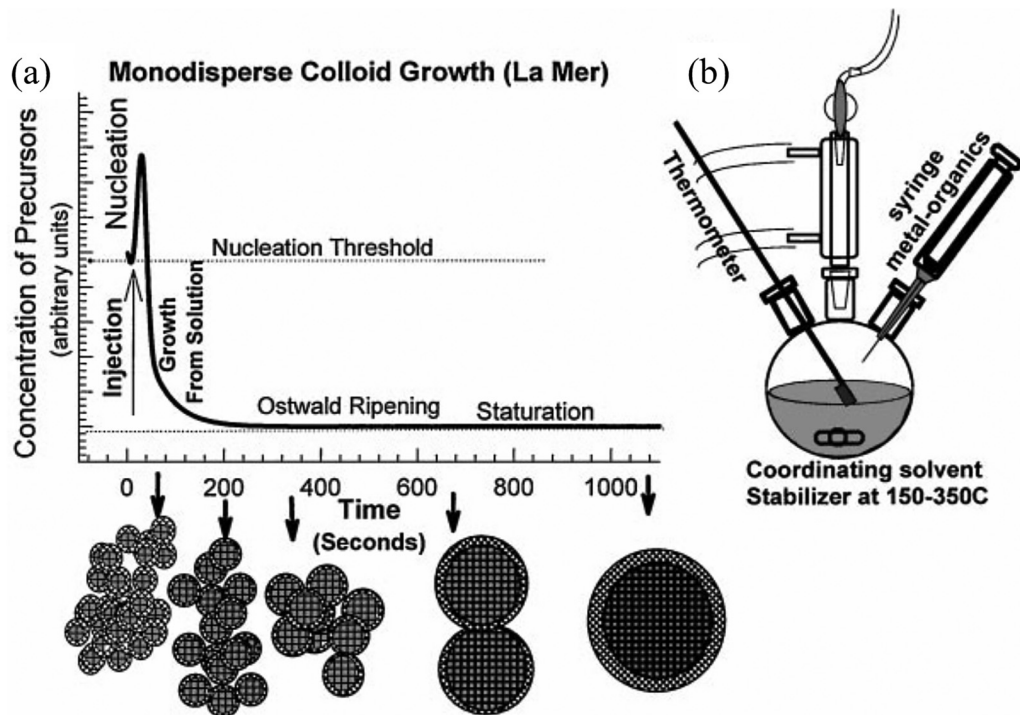


FIG. 1. (a) Schematic of La Mer and Dinegar's model for the synthesis of monodispersed CQDs. (b) Representation of the apparatus employed for CQD synthesis. Reproduced with permission from Murray *et al.*, Annu. Rev. Mater Res. **30**(1), 545–610 (2000). Copyright 2000 Annual Reviews.

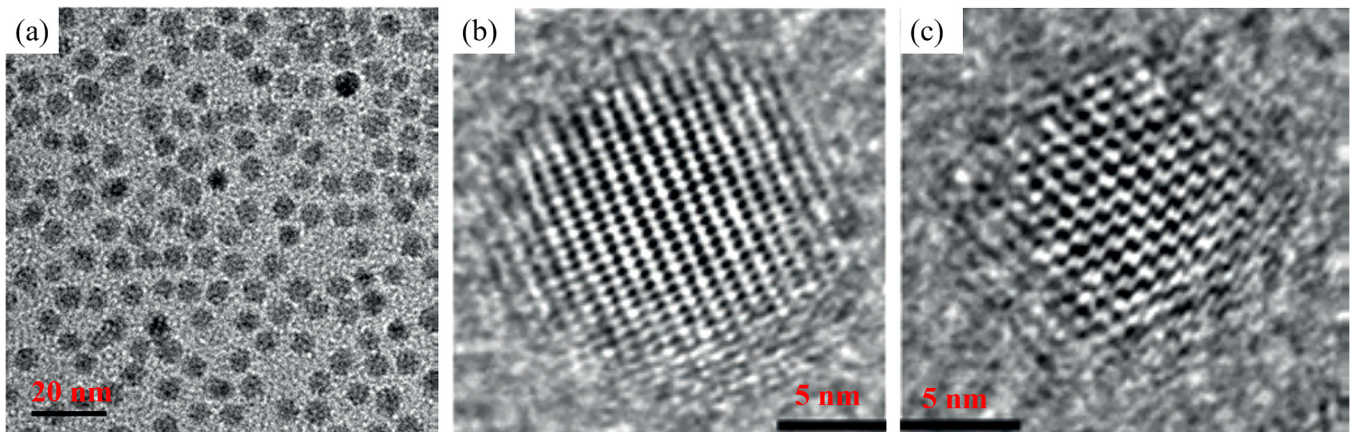


FIG. 2. Transmission electron spectroscopy (TEM) imaging of CdSe QDs: low resolution (a) and high resolution [(b) and (c)].⁷ Reproduced with permission from Kagan *et al.*, Nat. Nanotechnol. **10**(12), 1013 (2015). Copyright 2015 Nature Publishing Group.

to the further growth of large CQDs. In other words, the concentration of CQDs in the solution reduces with time, while the dot size increases, as shown in Fig. 1. However, La Mer and Dinegar's model for CQD synthesis is a simplified mechanism without considering the concurrence of semiconductor precursor nucleation and the CQD growth. Furthermore, ligands in the solution may additionally influence the nucleation process.

Besides, for better control of the CQD synthesis process, slow temperature ramping can be used to trigger the precursor supersaturation and nucleation. Furthermore, proper temperature control can also be implemented to avoid additional nucleation processes. As shown in Fig. 1, the CQD size can be feasibly adjusted by changing the hydrothermal fabrication time. Generally, this technique can fabricate CQDs with a dot size distribution of <7%, which can further be reduced to less than 5% through various purification methods. As an example, for CQD dimension measurement, the transmission electron spectroscopy images of CdSe CQDs at high and low resolutions are shown in Fig. 2.

2. Ligand exchanges and their effects on CQD carrier transport properties

With the reduction of CQD size, surfaces are starting to play an increasing role in determining CQD optical and electrical properties. For example, surface-to-volume ratios start to rise dramatically which leads to significant enhancement of surface trap states. Furthermore, large surfaces with high surface energy sensitively react with environmental chemical species, a process that diminishes CQD stability. Also, the as-fabricated CQDs are surface-linked with long organic molecules that result in large interdot distances corresponding to weak interdot coupling and thus to lower electrical carrier transport ability. Therefore, targeting the removal of surface trap states through satisfying unsatisfied dot surface dangling bonds and reducing interdot distances with short-chain linking molecules, surface ligand exchange is always performed. Examples of such ligands are tetrabutylammonium iodide (TBAI),

methylammonium lead iodide (MAPbI₃), and 1, 2-ethanedithiol (EDT), which have been widely used in fabricating CQDs for solar cell applications. Ligand exchanges are generally realized through solid-state layer-by-layer methods,⁸ while a solution-based ligand-exchange process was recently developed⁹ that enables the removal of original ligand organic molecules (oleic acid, for example). Compared with solid-state layer-by-layer exchange methods, solution exchange was demonstrated to have multiple benefits when applied to solar cell fabrication: reduced band-tailing improves open-circuit voltage, carrier transport, and charge injection into electron acceptors, and yields enhanced light absorption and an optimal CQD bandgap.⁹ It should be noted that in terms of the ligand-exchange process, there is a film thickness limitation that depends both on the ligand itself, the CQDs, as well as the ligand-exchange process. However, for better extraction of light-induced charge carriers in the film, the CQD film thickness is of the order of several hundred nanometers, a thickness enabling a desirable ligand-exchange performance.

CQD thin film electronic properties are multi-factor dependent, including interdot distance, the composition of QDs, number of neighbors, and linking ligands, all of which play key roles. Most of these factors are ligand determined. In a CQD thin film, as the interdot distance is reduced (e.g., through linking with ligands that have short chains), the wavefunctions of neighboring atoms overlap thereby strengthening interdot coupling. Coined as "artificial atoms," CQDs building blocks in thin films determine their material properties through their size, shape, the composition of each CQD, and the interdot distance.

As shown in Fig. 3(a), CQD ensembles with different interdot distances, short interdot distance (left) enable stronger coupling strength within neighboring dots. Therefore, the wavefunction overlap of neighboring CQDs transforms discrete electronic states into extended electronic states with a reduction of interdot distance. Accordingly, weak interdot coupling due to long linking ligands [Fig. 3(a), right] results in discrete electronic states. Ideal CQD thin films are truly monodisperse, i.e., all CQDs should have the same

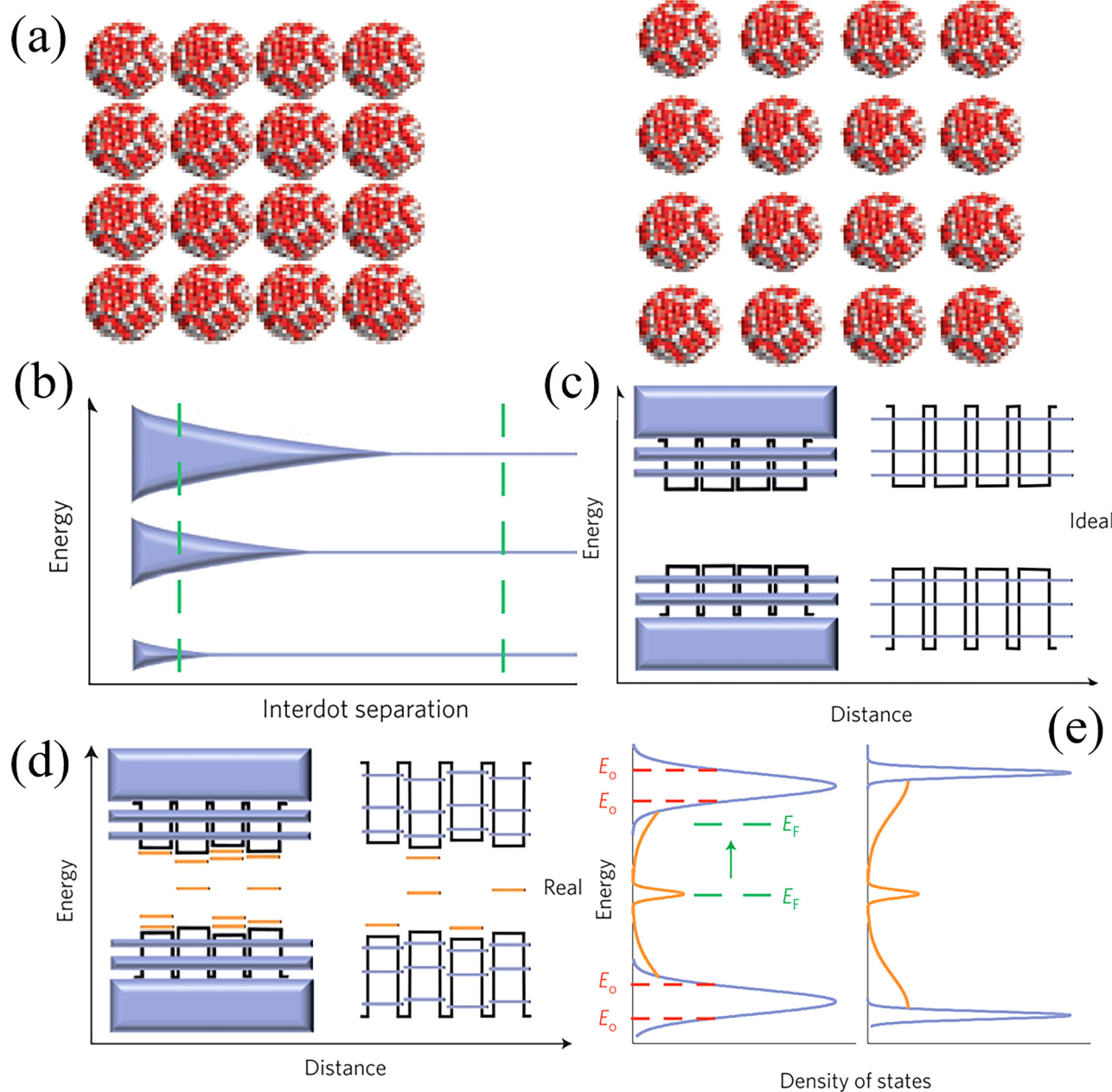


FIG. 3. Representations of CQD ensembles (a) with short interdot distance (left) and large interdot distance (right). Dependence of energy band on interdot separation (b). Energy band structure of ideal CQD ensembles (c) and real-world CQD ensembles (d) with the increase of interdot distance. The density of states (e) for coupled (left) and uncoupled (right) real-world CQD ensembles. Reproduced with permission from Kagan *et al.*, Nat. Nanotechnol. **10**(12), 1013 (2015). Copyright 2015 Nature Publishing Group.

size, composition, and shape, and all QDs should be in the same environment, for example, same charge and ligand chemistry. Furthermore, all dots are lodged in an ideal periodic matrix with the same interdot distance and number of nearest neighbors. In

this ideal situation, uncoupled CQD ensembles with large interdot distances possess degenerate electron and hole states as shown in Fig. 3(c) (right). In contrast, electronic states of coupled CQD ensembles results in bands from split states [Fig. 3(c), left].

TABLE I. Summary of the best-fitted parameters for CQD thin films surface passivated with various ligands. These parameters were evaluated for 100 K measurement. Reproduced with permission from Hu *et al.*, Sol. Energy Mater. Sol. Cells **164**, 135–145 (2017). Copyright 2017 Elsevier B.V.

Samples	PbS-EDT	PbS-TBAI	PbS-MAPbI ₃ -B	PbS-MAPbI ₃
Hopping diffusivity D_h (cm ² /s)	$1.62 \times 10^{-6} \pm 2.83 \times 10^{-8}$	$8.58 \times 10^{-7} \pm 3.74 \times 10^{-13}$	$8.82 \times 10^{-7} \pm 6.07 \times 10^{-14}$	$1.04 \times 10^{-6} \pm 3.93 \times 10^{-13}$
Effective carrier lifetime τ_E (μs)	$2.78 \pm 7.13 \times 10^{-6}$	$3.79 \pm 1.42 \times 10^{-8}$	$7.66 \pm 3.53 \times 10^{-8}$	$5.37 \pm 3.68 \times 10^{-8}$
Thermal emission rate e_i (s ⁻¹)	$6.53 \times 10^4 \pm 1.16$	$6.80 \times 10^4 \pm 0.000\ 86$	$4.96 \times 10^4 \pm 0.0010$	$6.70 \times 10^4 \pm 0.000\ 59$
Trapping rate R_T (s ⁻¹)	$4.72 \times 10^4 \pm 0.80$	$5.24 \times 10^4 \pm 3.71 \times 10^{-4}$	$2.04 \times 10^4 \pm 3.43 \times 10^{-4}$	$2.36 \times 10^4 \pm 8.99 \times 10^{-4}$
Absorption coefficient β (cm ⁻¹)	$8.57 \times 10^7 \pm 2.83 \times 10^6$	$6.22 \times 10^6 \pm 1.43$	$7.80 \times 10^6 \pm 0.34$	$2.79 \times 10^6 \pm 0.56$
Generation rate G_0 (cm ⁻³ s ⁻¹)	$1.84 \times 10^9 \pm 7.22 \times 10^7$	$1.81 \times 10^8 \pm 3.12$	$1.44 \times 10^8 \pm 2.50$	$3.04 \times 10^7 \pm 0.31$
Diffusion length L_h (μm)	0.017	0.018	0.026	0.024
Interdot spacing (nm)	0.43 (nominal ligand length)	3.50	3.30	3.30

For real CQD ensembles, the lowest size distribution that current synthetic methodology can achieve is around 5%. Along with the difference in ligand linking, composition, and variance in the interdot distance, these non-ideal factors dominate the inhomogeneity in the electronic states and give rise to the formation of midgap trap states. Furthermore, the inhomogeneity in the interdot distance and QD organization leads to a width and height distribution of the energy barrier between CQDs, thereby widening the distribution of electronic states as shown in Fig. 3(d). Figure 3(e) illustrates the density of states for real-world CQD ensembles. For uncoupled CQD thin films [Fig. 3(e) (right)], the density of states mirrors the energy and location disorder of the localized CQD states and midgap trap states. In comparison, the CQD energy bandwidth widening of electron and hole states originates from intra-state interactions.

As shown in Fig. 3, the bandtail states, the result of a disorder in CQDs and the interface states in devices, extend from the band edges into the bandgap and even into deep midgap states. For intrinsic CQD ensembles, if the Fermi level is located near the midgap within the deep localized states, charge carriers remain at the Fermi energy and transport occurs within localized states through hopping. However, due to chemical, electrochemical, or electrostatic doping, the Fermi energy is shifted close to the conduction band or valance band. As a consequence, deep level states are filled that lead to free carriers thermally excited into the extended states to enable a band-like electronic transport as shown in Fig. 3(e) (left). The authors have investigated the influence of ligands on the carrier transport properties of PbS CQDs.¹⁰ As shown in Table I, PbS CQDs are linked by means of various ligands: EDT, TBAI, and MAPbI₃, while the ligands lead to a CQD interdot spacing of approximately 0.43, 3.5, and 3.30 nm, respectively. As can be seen in Table I, hopping diffusivity increases with the decrease of CQD ligands.

B. Electrical properties of quantum dots

The transport of carriers including free charge carriers and excitons within QD thin films is of particular interest for the better understanding of fundamental carrier transport dynamics and energy loss mechanisms in QD systems and photovoltaic colloidal quantum dot solar cell (CQDSC) efficiency optimization. Section IA 2 reported on the influence of interdot linking ligands on

the QD electronic energy band structure and carrier transport behaviors. Short molecular lengths of linking ligands induce strong interdot coupling strengths, thereby forming an extended continuous energy band structure, which may result in an almost-continuous carrier transport behavior in QD systems with proper doping and negligible spatial and energy disorders. This section, starting with the discussion of the theoretical background on carrier transport between localized states, discusses the dependencies of carrier transports in CQD thin films on temperature, interdot distance associated coupling strength, dot size, QD size polydispersity, and spatial and energy disorder.

1. Theoretical fundamentals of carrier transfer between localized states

The relevant theory of electron transfer in localized states was initially developed by Marcus¹¹ with the consideration of initial and final states as a function of the nuclear coordinates as shown in Fig. 4. For electron transport in QDs, Marcus' theory takes into account the free energy change ΔG^0 for electron transport from the initial state to the final state and the reorganization energy λ in response to the nuclear coordinate change during the transport process. The reorganization energy λ is determined by the internal vibrations of the molecules and the configuration changes of the solvent or dielectric materials that surround the molecules.

Carrier transport between localized states in QDs that contain photoexcited electrons and holes is quantitatively modeled through their tunneling behavior under a one-dimensional potential approximation in the presence of an applied electric field as reported by Leatherdale *et al.*¹² The tunneling probability can be obtained by implementing the Wentzel–Kramer–Brillouin (WKB) approximation in a model where electrons tunnel through a square energy barrier of height Φ and width d in an applied field E ,

$$S = \exp \left\{ -\frac{4}{3} \sqrt{\frac{2m^*}{\hbar^2}} \frac{1}{eE} [\Phi^{3/2} - (\Phi - eEd)^{3/2}] \right\}, \quad (1)$$

where m^* is the effective mass of the transport carrier within the energy barrier. It can be seen that the tunneling probability decreases exponentially with increasing energy barrier width, which is significantly determined by the linking-ligand-associated interdot spacing.

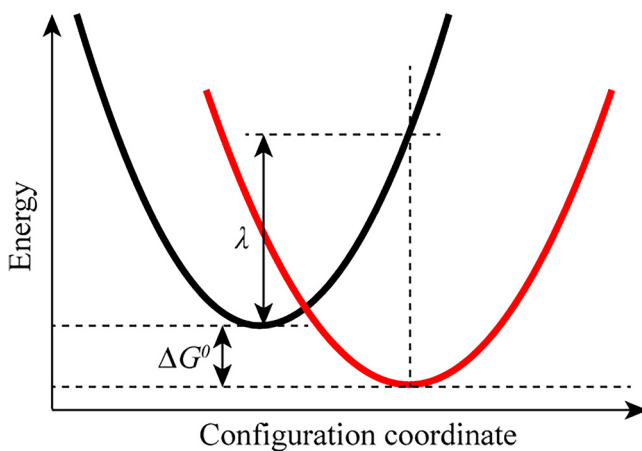


FIG. 4. Schematic of the energy diagram to illustrate Marcus' theory for electron transport between localized states. ΔG^0 is the free energy change for transport from the initial to the final state, and λ is the reorganization energy required to change when the nuclear configuration coordinate changes adjusting to the transport.

Carrier mobility is an essential carrier transport property; therefore, it is a system where the hopping transport is dominant such as in QD systems, its definition needs to be revisited¹³ within the framework of discrete hopping transport as a function of the electric field and the electric-field-dependent net hopping rate, $R(E)$,

$$\mu(E) = \frac{R(E)}{E} d, \quad (2)$$

where d is the hopping distance along the direction of the electric field and equals the nearest neighbor (interdot) hopping (NNH) distance. The net hopping rate $R(E)$ can be further defined as the difference between forward (hopping in) and backward (hopping out) rate, i.e.,

$$R(E) = R_{\text{forward}}(E) - R_{\text{back}}(E). \quad (3)$$

Taking into account trapping states that may be occupied by a significant amount of charge carriers and render them completely immobile, the definition Eq. (2) should be modified with the definition of effective carrier mobility $\mu_{\text{eff}}(E)$,

$$\mu_{\text{eff}}(E) = \mu_{\text{free}} \frac{n_{\text{free}}}{n_{\text{total}}}. \quad (4)$$

The term n_{total} denotes the total density of trapped and free carriers while n_{free} is the density of free carriers. Besides, μ_{free} is the mobility of free carriers.

In general, in CQDs, depending on the specific surface passivation ligands, significant effects of trapping states emerge due to the small-dot-size-related high surface-to-volume ratio. The model described by Eq. (4) is too simplistic when considering various trap states with different energy levels because carriers cannot be

distinguished as mobile and immobile depending on whether they are not trapped or trapped, respectively. Specifically, there exist some shallow traps that capture carriers rendering them only less mobile relatively to free carriers. In this case, where there exists a population of carriers n_i with different mobilities μ_i , therefore, a more appropriate approach to defining mobility is as follows:

$$\mu_{\text{eff}} = \frac{\sum_i \mu_i n_i}{\sum_i n_i}. \quad (5)$$

Furthermore, the quantized high energy states have not been considered. According to the Marcus theory, at high electric fields, electrons are more likely to be injected into higher-lying electronic states, followed by rapid relaxation to lower states.¹⁴ Therefore, high energy state occupation results in smaller activation energies for electron transport between localized states compared with direct transport within low energy states.

2. Effects of interdot distance and QD disorder

Depending on the degree of QD disorder with respect to spatial arrangements and energy states, there are four possible transport mechanisms as shown in Fig. 5.¹⁵ Strictly speaking, at room temperature, without specifying materials and quantitative calculation processes, all four transport mechanisms are possible.

First, bulk crystal-like Bloch states will be formed when the inter-dot distance is very small [Fig. 5(a)], and the whole QD matrix has a quasi-monodispersed dot size. In this case, the strong coupling strength causes carrier wavefunctions to overlap leading to a narrow continuous energy band of a certain range in QD thin films. Crystal-like Bloch states are not common in real practical QD samples due to the inevitable CQD polydispersity even from today's state-of-the-art fabrication techniques as discussed in Sec. I A 1. In the crystal-like Bloch states with extended energy bands, excitons dissociate into free electrons and holes immediately upon generation due to the strong interdot coupling strength. Second, quantum mechanical tunneling becomes the dominant carrier transport mechanism with increasing interdot distance or dot size polydispersity [Fig. 5(b)] [compared with the situation in Fig. 5(a)]. In this situation, charge carriers can be transported from one QD to its neighbors without phonon assistance due to the strong interdot coupling. It is well known that, due to the energy barrier present in between, charge carriers cannot be transported from one quantum dot to another if there are far apart from each other. However, if two quantum dots are very close (passivated with short ligands, for example), these two dots are strongly coupled as determined by the spatial overlap of their wavefunctions, each of which penetrates through the energy barrier. Given the probabilistic nature of the electronic wavefunction, this means that there is a finite probability that the carriers can appear on (be transported, or "tunneled" through to) the opposite side of the potential barrier. Indeed, it has been reported that tunneling occurs with barriers of thickness around 1–3 nm or thinner, a distance that is very common for CQD thin films.

Third, when the energy barrier between neighboring QDs is low enough [Fig. 5(c)], carriers can be thermally excited and transported over the barrier. For CQD systems, this mechanism allows

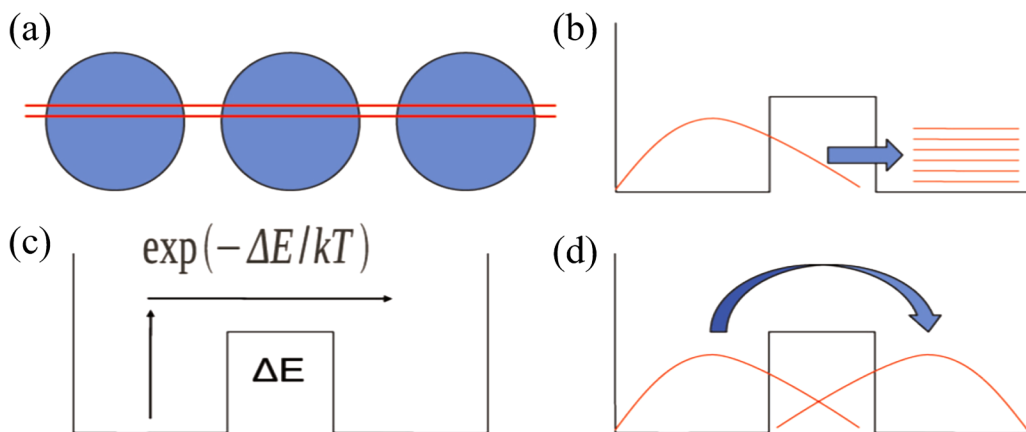


FIG. 5. Various carrier transport mechanisms for QD thin film systems: (a) bulk crystal-like Bloch state carrier transport; (b) carrier tunneling transport from one dot to another without phonon assistance; (c) carrier transport with over-the-barrier activation energy mechanism; and (d) hopping transport with phonon assistance. Reproduced with permission from Chu *et al.*, Annu. Rev. Phys. Chem. 115(43), 21409–21415 (2011). Copyright 2011 Annual Reviews.

carriers to be transported freely over the energy barrier from one QD to another. Fourth, the phonon-assisted hopping mechanism is most widely encountered in QD systems [Fig. 5(d)].^{16–22} For photon-assisted hopping, the electron hops from one dot to a nearby dot by absorbing one or multiple phonons. Depending on interdot distance, coupling strength, temperature, and QD dimension, carriers hop from one dot to the nearby dots with the assistance of one or multiple phonons. As the population of phonons is temperature-dependent, phonon-assisted hopping transport is also temperature-dependent, thereby leading to increased mobility and conductivity with increasing temperature, a behavior that stands in stark contrast to that of bulk semiconductors with continuous energy bands.

In summary, the interdot coupling strength that increases with reduced ligand-determined interdot distance has a significant influence on carrier transport physics. Through the enhancement of the interdot coupling strength, it has been found that the electrical properties of QD systems evolve from a Coulomb blockade dominated insulating regime to a hopping conduction dominated semiconducting regime in QDs.^{16,23} Strong interdot coupling strength can also assist exciton dissociation into free electron and hole charge carriers during the tunneling or hopping processes.^{24,25}

3. Temperature effects

With decreasing temperature, the QD carrier transport mechanism evolves from nearest-neighbor hopping (NNH) to Efros-Shklovskii-variable-range hopping (ES-VRH). The watershed temperature for one mechanism to the other has been reported to be ~ 200 K,^{17,19,21} while further investigation found that the watershed temperature could be affected by the QD size.¹⁹ NNH and ES-VRH exhibit temperature-dependent effects on device current density or conductivity similar to phonon-assisted carrier hopping transport, i.e., at high temperatures, the large phonon population facilitates the carrier hopping transport mechanism.^{16,19,20} The dependence

of conductivity on temperature for hopping conduction takes on the general form

$$\sigma = \sigma_0 \exp[-(T^*/T)^z], \quad (6)$$

where σ_0 is the conductivity pre-exponential factor, T^* is a fitting parameter with units of degrees Kelvin, and z is a parameter associated with different hopping transport mechanisms. Specifically, as shown in Fig. 6, when $z=1$, carrier transport across CQDs takes place through NNH, while $z=0.5$ corresponds to ES-VRH. Moreover, for Mott variable-range hopping (M-VRH),²⁵ z is equal to 0.25 in a three-dimensional transport model and is equal to 0.3 for a two-dimensional transport model.

M-VRH is the dominant carrier transport for CQD systems at low temperatures within strongly disordered systems that have localized states. Carriers in an initial state of energy E_i are thermally activated and hop to a nearby energy state with a final state energy E_f . The hopping probability is given by Eq. (1) as a function of the state energy difference $\Delta E = E_i - E_f$ and hopping distance d , i.e., a larger energy difference between the two states combined with a shorter hopping distance facilitate the M-VRH hopping process as shown by carrier hopping paths I and II in Fig. 6. Instead, NNH is most likely to occur at high temperatures such as the hopping path I in Fig. 6 from a 1Se state in CQD 1 to another 1Se state or a trap state in CQD 2; or a hop between trap states from CQD 3 to CQD 2. As for the ES-VRH, the quantum localization length is assumed to be much smaller than the spatial distance between centers, and the overlap between the wave functions is neglected.

If the energy difference ΔE is equal to the Coulomb gap energy δ , the conductive mechanism changes from ES-VRH to M-VRH. For weakly coupled QDs, the Coulomb gap energy can be approximated by $\delta \approx 2E_c$, where E_c is the charge ionization energy, i.e., the energy required to add or remove a charge carrier from a QD, which can be estimated for a spherical QD through the

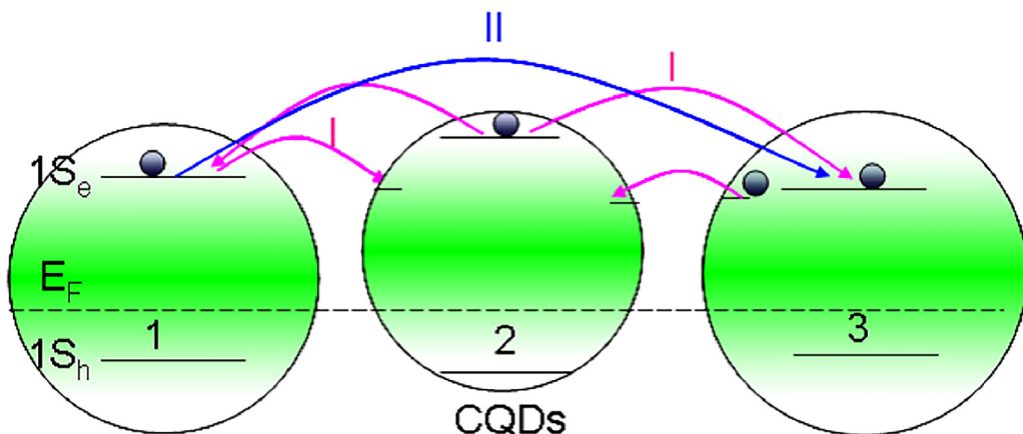


FIG. 6. Schematic of charge carrier transport across a colloidal quantum dot array. Energy states, including trap states and Fermi levels, are represented by solid and dashed lines, respectively. Nearest-neighbor hopping (I) and variable range hopping (I + II) occur through carrier transport in quantized states (solid lines, $1S_e$ and $1S_h$ for electrons and holes, respectively) and surface trap states (solid lines). Variation in quantum dot sizes creates energy and spatial disorder that weakens interdot coupling and perturbs carrier transport. Reproduced with permission from Tang *et al.*, *Adv. Mater.* **23**, 12–29 (2011). Copyright 2011 Wiley-VCH.

electrostatic formula

$$E_c = \frac{e^2}{4\pi\epsilon r}. \quad (7)$$

Here, r is the radius of the QD, e is the elementary charge, and ϵ is the permittivity of the material in which the QD system is located. Romero and Drndic¹⁶ used the aforementioned model to study carrier transport in PbSe CQDs with surface capped with oleic acid. It was found that for CQD thin films annealed at a lower temperature (373 K) in vacuum, Coulomb blockade is the dominant effect in carrier transport. It leads to the well-known insulating conductivity property of PbSe CQD thin films due to the higher charge energy E_c of 36 meV than the thermal energy of ~32.5 meV at 373 K. In contrast, under high annealing temperatures (such as 473 K), the interdot distances were reduced, a fact that led to conductive electrical property.¹⁶ As shown in Fig. 7, fitting the conductivity to Eq. (6) reveals a z value of 0.95–1.05 and 0.48–0.55 for high and low temperatures, respectively, which imply M-VRH carrier hopping at high temperatures and E-VRH at low temperatures.

4. Effects of quantum dot size and polydispersity

In QD thin films, different types of charge carriers exhibit different transport behavior, which also depends on the QD size. Lee *et al.*²⁶ and Liu *et al.*¹⁸ found that both electron and hole mobilities increase by 1–2 orders of magnitude with increasing PbSe QD size. Specifically, further investigations show that electron mobilities decrease for QDs with large diameter, exhibiting a mobility peak at ~6 nm QD diameter. In contrast, hole mobility exhibits a monotonically increasing behavior. Carrier mobility increases with QD diameter can be attributed to the reduced activation energy in larger QDs, while the decrease of electron mobility for larger QDs

may be due to weaker electronic coupling strength among larger QDs as discussed by Lee *et al.*²⁶ The electron and hole hopping mobility dependencies on QD size of PbSe quantum dots are shown and compared in Fig. 8.²⁶ Particularly, the computed electron mobilities agree well with the experimental counterparts that have an interdot distance corresponding to the length of the ethane dithiol ligand. Furthermore, it can also be seen from Fig. 8 that mobility is also inter-dot distance dependent. With a shorter inter-dot distance, such as 0.5 nm, higher mobility is observed in the CQD thin film when compared with CQDs with a 0.6 nm and 0.7 nm interdot distance. Furthermore, both electron and hole mobilities decrease exponentially with increases in ligand length as predicted by Eq. (1), consistent with the hopping/tunneling transport mechanism: short interdot distance results in higher coupling strength and narrower barrier width.

QD size polydispersity deteriorates the interdot coupling strength, thereby affecting charge carrier transport. Due to the quantum confinement effect, within a CQD ensemble, CQDs of different sizes correspond to different bandgap energies; therefore, size polydispersity results in a bandgap energy range. Meanwhile, big QDs with high bandgap energy can act as carrier trapping states. For QDs with a given/fixed density of surface trap states, Liu *et al.*¹⁸ discovered that the carrier mobility is independent of QD size polydispersity. Zhitomirsky *et al.*²⁷ also reported that the QD polydispersity had a negligible impact on photovoltaic device performance with a fixed concentration of surface traps. However, upon significant reduction of surface trap densities, further studies showed that an improved photovoltaic device performance was achieved with the successful decrease of QD size polydispersity.²⁷

To summarize, as discussed above, properties of CQD and CQD-based solar cells are multiple-parameter dependent and their electrical behaviors differ significantly from those of their counterpart Si materials and Si-based solar cells. Table II compares various relevant parameters including intrinsic carrier concentration, solar

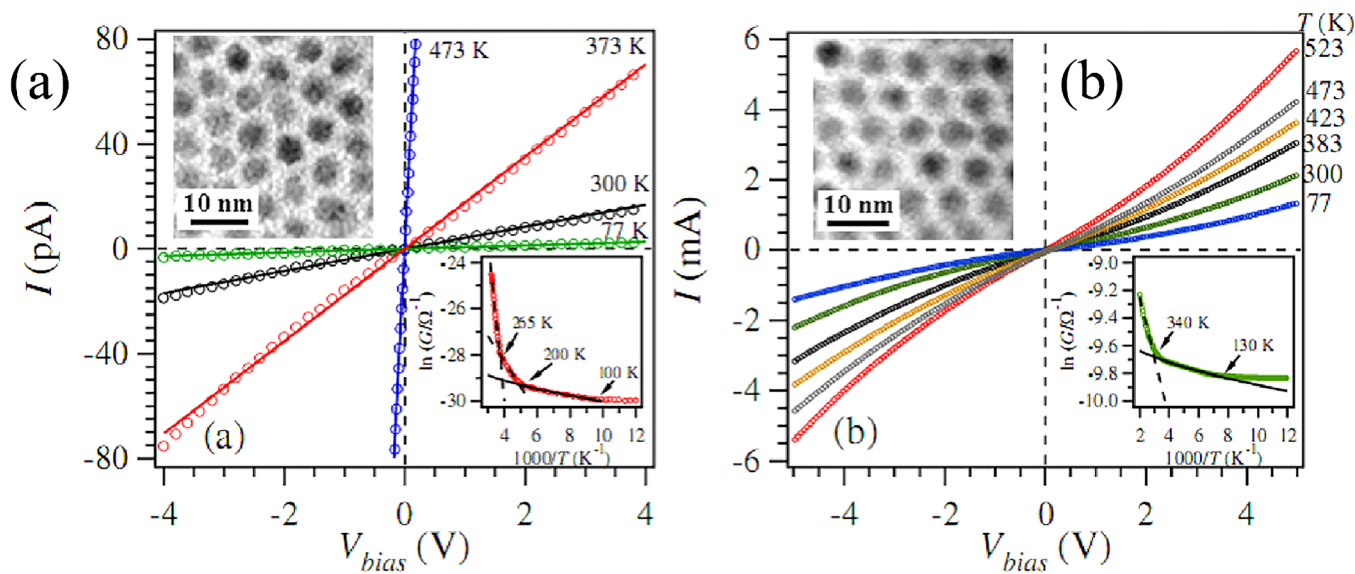


FIG. 7. Current-voltage characteristics at several temperatures for PbSe CQD thin films vacuum-annealed at 473 K (a) and 523 K (b). The low-right insets in both figures show Arrhenius plots of conductivity G the same as σ in Eq. (6), and the upper-left insets depict TEM images of PbSe CQD arrays after vacuum annealing. Reproduced with permission from Romero *et al.*, Phys. Rev. Lett. **95**(15), 156801 (2005). Copyright 2005 American Physical Society.

cell thickness, diffusion length, diffusivity, mobility, bandgap energy, and carrier lifetime between CQD and Si solar cells. These two types of semiconductor materials have dramatically different properties due to their fundamentally different material structure and carrier transport parameters. In terms of solar cell efficiency, Si solar cells currently are superior to CQD solar cells, while the latter are low-cost due to their solution-processing fabrication method and can be spray-coated on variable low-cost substrates where Si cannot.

C. Colloidal quantum dot solar cells

1. Classification and fundamentals of colloidal quantum dot solar cells

a. Classification. Colloidal quantum dot solar cells (CQDSCs) have attracted considerable attention due to their much higher theoretical solar energy to an electricity conversion efficiency of $\sim 44\%$ than the Shockley–Queisser limit for Si solar cells (33%),^{34–37}

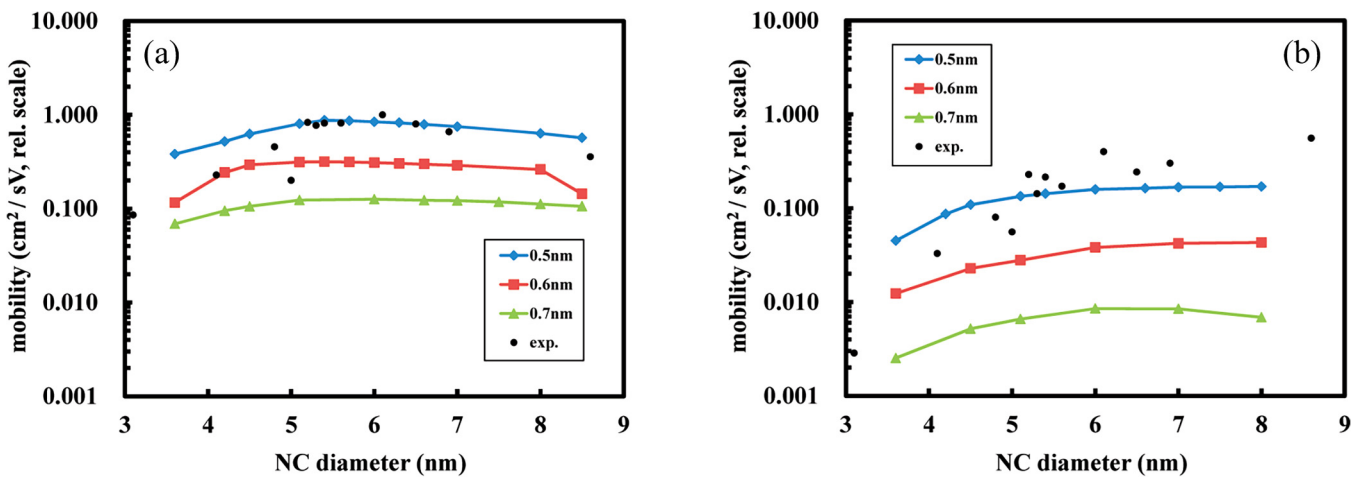


FIG. 8. Experimental and modeled electron (a) and hole (b) mobility of PbSe QDs, at a different interdot distance, i.e., 0.5, 0.6, and 0.7 nm in the figure legend, and as a function of QD diameter. Reproduced with permission from Lee *et al.*, J Phys. Chem. Lett. **6**, 714–719 (2012). Copyright 2012 American Chemical Society.

TABLE II. Carrier transport parameters for CQDSC and Si-based solar cells (Si-SC).

Parameters	CQDSC	Si-SC	Reference
Intrinsic carrier concentration, $n(0)$	$1 \times 10^{16} \text{ cm}^{-3}$	$1.5 \times 10^{10} \text{ cm}^{-3}$	28, 29
Solar cell thickness	$0.41 \mu\text{m}$	$100\text{--}500 \mu\text{m}$	9
Diffusion length	350 nm	$100\text{--}300 \mu\text{m}$	9, 30
Diffusivity	$1 \times 10^{-4}\text{--}0.02 \text{ cm}^2/\text{s}$	$\leq 36 \text{ cm}^2/\text{s}$ (electron), $\leq 12 \text{ cm}^2/\text{s}$ (hole)	10, 31
Mobility	$1 \times 10^{-3}\text{--}10 \text{ cm}^2/\text{V s}$	$\leq 1400 \text{ cm}^2/\text{V s}$ (electron), $\leq 450 \text{ cm}^2/\text{V s}$ (hole)	28, 32
Bandgap energy	0.5–3.6 eV	1.11 eV	32
Carrier lifetime	0.1–5 μs (typical)	$\sim 1 \text{ ms}$	10
Highest efficiency	16.6%	27.6%	33

tunable QD bandgap energy through effective dot size control, and solution-mediated fabrication that is suitable for low-cost, flexible, lightweight, large-area solar cells.

Two types of QD solar cells are most popular and under intensive study: QD-sensitized and QD heterojunction solar cells. Although CQDSCs have been fabricated with various architectures, typical types have four main components: a transparent

conduction electrode [ITO and fluorine doped tin oxide (FTO)], a metal oxide semiconductor thin film with thickness from tens of nanometers to several hundred nanometers, light-absorbing CQD thin films of several hundred nanometers or thinner (depending on the carrier diffusion length), and a metal electrode such as Au. The first generation of CQDSCs was Schottky solar cells as shown in Figs. 9(a) and 9(b).³⁸

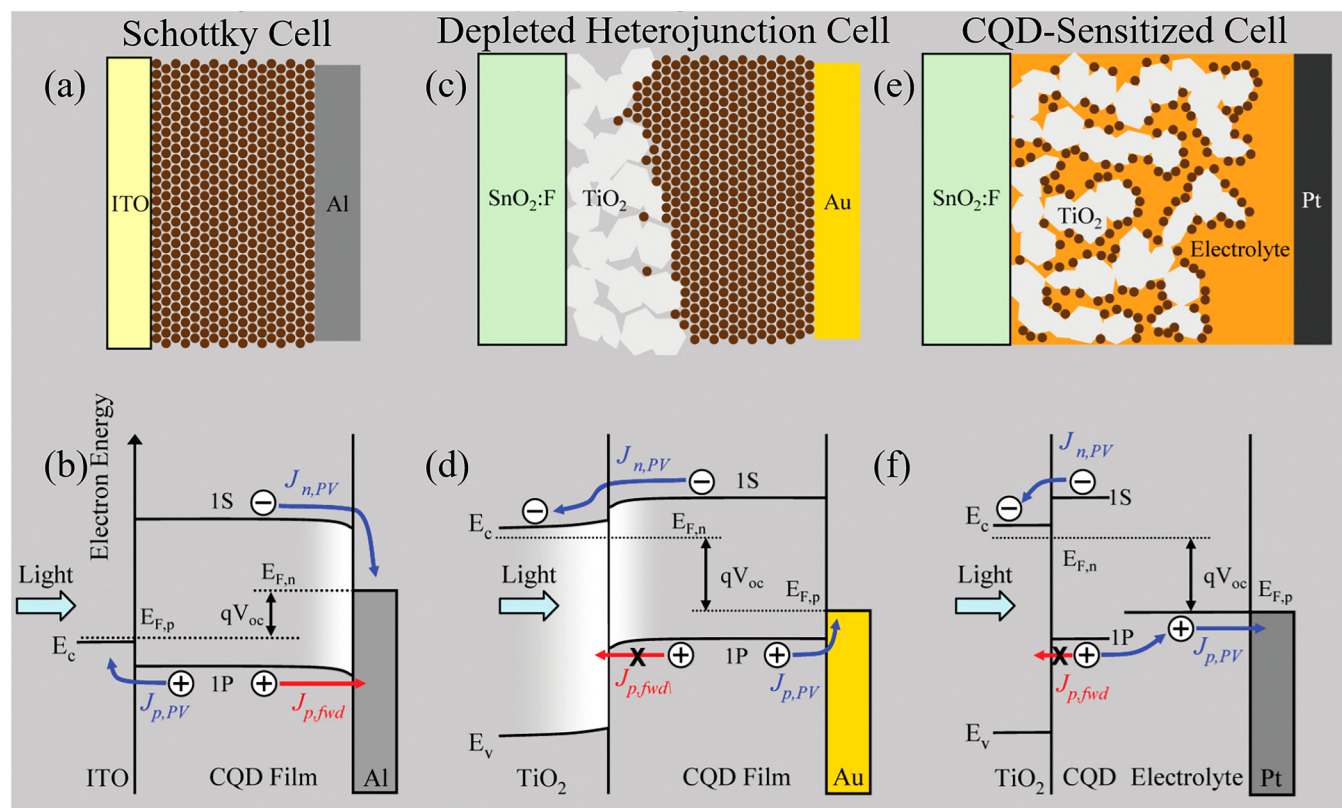


FIG. 9. Configuration of different types of CQDSCs: Schottky [(a) and (b)], heterojunction [(c) and (d)], and CQD sensitized solar cells [(e) and (f)]. The top row [(a), (c), and (e)] illustrates the device structure and the bottom row [(b), (d), and (f)] depicts the energy band structures with carrier transport mechanisms displayed. Only the lowest energy states are shown (i.e., 1S and 1P) for simplification. Reproduced with permission from Pattantyus-Abraham *et al.*, ACS Nano 4(6), 3374–3380 (2010). Copyright 2010 American Chemical Society.

The Schottky diode formed at the electrode/CQD thin film interface leads to a depletion region with an intrinsic electric field that can drive electron and hole transport to the Al (anode) and ITO (cathode) electrodes, respectively. CQD thin films are the light absorption layer that generates excitons with photoexcitation. The photoexcited excitons diffuse along their density gradient from the ITO layer where the excitation light impinges. The interdot coupling electric field strength can separate these excitonic electron-hole pairs into free charge carriers. Furthermore, excitons can also dissociate at the CQD/Al interfaces; however, this limits device efficiency as hole charge carriers need to travel all the way back to the ITO electrode. Figure 9(b) shows that the dissociated electrons need to diffuse in the quasi-neutral region and drift in the depletion region to reach the Al electrode to be subsequently extracted outside. The open-circuit voltage V_{oc} is a function of the energy difference between the quasi-Fermi levels of electrons and holes in the form

$$V_{oc} = \frac{E_{F,n} - E_{F,p}}{q}, \quad (8)$$

where $E_{F,n}$ and $E_{F,p}$ are the quasi-Fermi levels for electrons and holes, respectively. For metal electrodes, the quasi-Fermi level is determined by the work function of the corresponding metal, as can also be seen in Fig. 9. Schottky-diode-based CQDSCs suffer from low fill factors

(FFs) and V_{oc} for a given J_{sc} . Besides, as shown in Fig. 9(b), hole charge carriers can be injected into the electron extraction electrode because of the poor energy barrier formed by the Schottky diode, which results in enhanced carrier recombination and decreased CQDSC efficiency. In comparison, QD-sensitized solar cells consist of a QD-sensitized photoelectrode [TiO_2 , Figs. 9(e) and 9(f)] and a counter electrode, and they are separated by a liquid electrolyte. These QDs act as light absorbers; however, due to the thinness of these QD layers, QD-sensitized solar cells suffer from low-light-absorption-induced poor J_{sc} albeit with appreciable FF and V_{oc} . Heterojunction CQDSCs [Figs. 9(c) and 9(d)] follow a similar carrier extraction mechanism as Schottky-diode-based CQDSCs except for additional exciton dissociation sources from the heterojunction interfaces. Metal oxide materials such as TiO_2 and ZnO in nanostructures are often used as the nominal n-type component of the heterojunction p-n structure. The depleted heterojunction structure can simultaneously maximize FF, V_{oc} , and J_{sc} ; therefore, CQDSCs with high efficiencies have such a heterojunction structure albeit with different QD materials or electrodes.

Typically, there are two types of heterojunction CQDSCs: the planar depleted heterojunction and bulk heterojunction.^{39,40,41} Figure 10 shows the device structures and working principles of these two kinds of heterojunction CQDSCs. Planar heterojunction solar cells have the typical structures discussed above and are

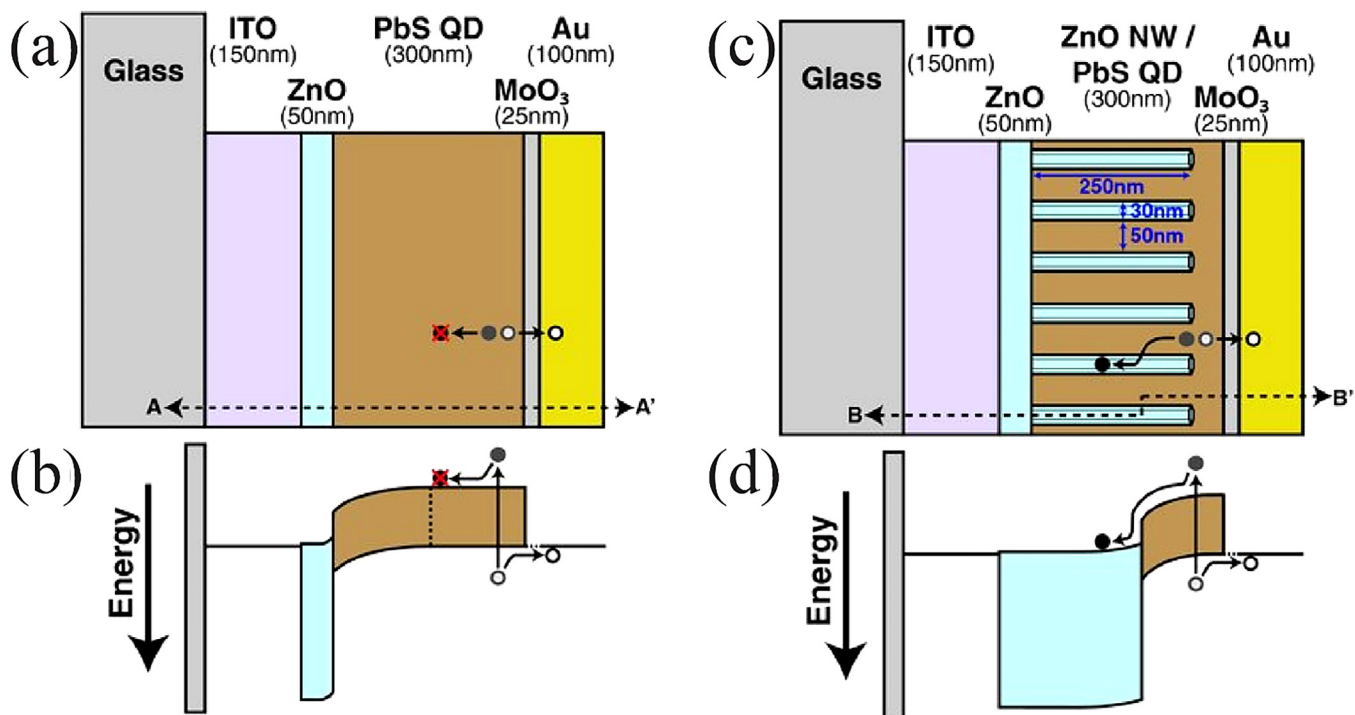


FIG. 10. Schematic (a) and energy band diagram (b) of the planar depleted CQD heterojunction solar cell at short circuit. The energy diagram is plotted along the A–A' cross section. Correspondingly, the schematic (c) and energy diagram (d) (a cross section along B–B') for bulk heterojunction. The vertical ZnO nanowires were grown using solution-processed hydrothermal methods to produce an ordered nanowire array within the PbS CQD thin film. Reproduced with permission from Jean et al., *Adv. Mater.* **25**, 2790–2796 (2013). Copyright 2013 Wiley-VCH.

shown in Figs. 9(e) and 9(f). Figures 10(a) and 10(b) showcase the planar CQDSC heterojunction consisting of ZnO and PbS CQDs. The depletion region is formed and centered at the ZnO/CQD thin film interface and extends into the CQD thin films. To harvest more charge carriers for high J_{sc} , high-efficiency CQDSCs need to absorb more light, a process that depends directly on the light-absorbing thickness of the CQD thin film. However, the thickness of CQD thin films is limited by the exciton or free charge carrier diffusion length (generally speaking, several hundred nanometers) as carriers need to travel across the entire thin film to be extracted by the respective electrodes. Therefore, the light-absorbing CQD layer thickness is limited by the carrier diffusion length which, in turn, restricts the enhancement of short-circuit current density J_{sc} .

Bulk junction CQDSCs have emerged as attempts to increase J_{sc} through architectural design. In general, bulk heterojunction CQDSCs are established using pillars⁴¹ or nanowire arrays^{39,42–46} with interpenetrated CQDs. These pillars and nanowires are generally nanostructured metal oxides including ZnO and TiO₂. One of the advantages of the bulk heterojunction is the ability to extend the depleted regions to several micrometers, which leads to enhanced charge separation and collection efficiency. Using bulk heterojunction CQDSCs, obvious improvement of J_{sc} as high as 30 mA/cm²^{42,43,47} have been reported. However, the overall CQDSC efficiency is not profoundly improved due to the loss of V_{oc} from enhanced carrier recombination due to additionally increased CQD/metal oxide interfacial trap states. Nevertheless, bulk heterojunction CQDSCs hold great promise for performance optimization with respect to increased J_{sc} when CQD and interface quality are significantly improved in the future. Approaches to suppressing interfacial carrier recombination are discussed in Sec. I A 2.

b. CQDSC fundamentals. A quantitative description of CQDSC working principles, for example, J - V characteristics, should be different from that of conventional Si solar cells due to: (a) spatial and energy-disorder-induced non-continuous energy bands (as discussed in Sec. I A 2), which lead to discrete hopping/tunneling based carrier transport and (b) much lower carrier mobility (10^{-5} – 10^{-1} cm²/V s for CQD thin films, compared to 10^2 – 10^3 cm²/V s for conventional Si wafers). The latter issue renders the S-Q equation invalid when used for such low-mobility systems.^{48,49} For solar cell J - V characteristics, the dark current reflects the natural properties of the solar cell diode. Ideally, the current density under illumination is the result of dark current shifted by the photogenerated current, which leads to the classical J - V characteristics with a power conversion efficiency (PCE) expressed as

$$\text{PCE} = \frac{V_{max} J_{max}}{P_{inc}} = \frac{V_{oc} J_{sc} FF}{P_{inc}}, \quad (9)$$

where V_{max} and J_{max} are the voltage and current density, respectively, at maximum solar cell power and P_{inc} is the total intensity of the incident light. A review of other fundamental photovoltaic equations can be found elsewhere;²⁵ however, these formulas hold for conventional solar cells by virtue of the continuous carrier transport behavior in those devices but not widely used in QD-based solar cells due to the reasons discussed above. Therefore,

they are beyond the scope of this review article and are not discussed further here.

2. New concepts for improving CQD solar cell efficiency

a. Harvesting hot carriers and MEG. For a review of experimental approaches, efforts made until now for CQDSC efficiency optimization are focused on the increase of either photovoltage (V_{oc}) or photocurrent density (J_{sc}). Efforts are mostly through the use of materials science to improve CQD quality or through physical energy band engineering to reduce interface-associated energy dissipation. To enhance V_{oc} , effective harvesting of the excess kinetic energy of hot carriers before they decay (relax) to the energy band edge is also a promising approach that has attracted considerable attention. Figure 11 shows the schematic of a hot carrier solar cell working principle. Specifically, photoexcited electrons and holes generally possess excess kinetic energy.³⁵ They quickly thermalize by relaxing through the transfer of energy to phonons with the generation of heat. After thermalization to the respective band edge, the maximum solar cell $V_{oc} = E_g/q$ becomes bandgap limited without considering trap states. Hot carrier solar cells harvest hot carriers before their cooling down to the band edges and extract these carriers over a narrow range of energy, δE in Fig. 11. In this manner, V_{oc} is no longer bandgap limited and can be significantly enhanced as shown in Fig. 11.

The kinetic energy of hot carriers is defined here as the difference between the excitation photon energy and the solar cell bandgap energy. Hot carriers are defined according to their effective temperature when taking into account their kinetic energy. Generally, effective temperatures for hot electrons and holes are

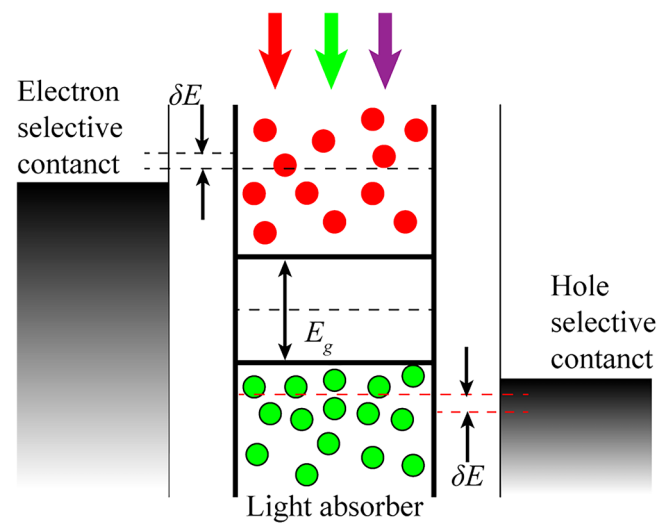


FIG. 11. Schematic of a hot carrier solar cell energy band structure. Through harvesting of hot carriers before they thermalize to the band edges, the open-circuit voltage is significantly augmented.⁵⁰ Reproduced with permission from Le Bris *et al.*, Appl. Phys. Lett. **97**, 113506 (2010). Copyright 2010 AIP Publishing LLC.

around 3000 K, which is much higher than the normal lattice temperature of 300 K.

As a consequence, hot carrier solar cells can reach a theoretical efficiency enhancement as high as 68%. The harvest of hot electrons depends on three rates: extraction rate (i.e., the rate of hot carriers to be extracted at the electrodes), MEG rate (i.e., the kinetic-energy-induced additional exciton generation with a prevailing mechanism of impact ionization), and the rate of hot carrier cool down to the semiconductor band edge. For the effective harvest of hot carriers, the above rates must satisfy the following stringent conditions: (1) the hot carrier cooling rate (i.e., photocarrier thermalization rates) in the photon absorbing layers, i.e., the CQD layers for CQDSCs, should be slow and (2) the extraction rate at the electrodes should be high and the extraction should be over a narrow range of energies to avoid energy loss to cold contacts. Furthermore, as a consequence of the competitive nature of these rates, hot carrier transport or collection and MEG cannot occur simultaneously. Furthermore, the excess kinetic energy of hot carriers can also be used for MEGs with the creation of additional electron-hole pairs, so that J_{sc} increases. As MEG has already been discussed in detail in Ref. 36, it will not be repeated here. Both of these two approaches MEG and hot carrier solar cells show excellent promise for improving the CQDSC efficiency dramatically.

Recently, hot carrier extraction and MEG have been studied in CQDs to improve photovoltaic CQDSC efficiency. However, no direct applications of MEG toward enhancing CQDSC efficiencies have been reported to-date. The Guyot-Sionnest group studied hot carriers in CQDs^{51,52} to slow the hot electron energy loss to the lattice vibration for more efficient photovoltaic or infrared devices. As discussed in Refs. 35 and 36, hot carrier relaxation should be slow in QDs due to their well-separated discrete electronic states. Pandey and Guyot-Sionnest⁵¹ measured a slow intraband relaxation of more than one nanosecond in colloidal core/shell quantum dots. This decay time depends on the QD structure and varies from less than 6 ps to longer than 1 ns with different shell composition and thickness. Pandey and Guyot-Sionnest⁵² further studied hot electrons through the generation of hot carriers in core/shell CdSe/ZnSe CQDs using mid-infrared intraband excitation. Time-resolved visible-range spectroscopy was used for probing hot electrons. It was found that hot electrons were excited to the first excited conduction state 1 Pe (denoting the p orbital based electron states) of the CQD core, and were subsequently efficiently extracted through the ZnSe shell. The electron extraction times were measured to be shell thickness-dependent ranging from 4 to 100 ps. Tisdale *et al.*⁵³ demonstrated the possibility of hot electron transfer from semiconductor CQDs to a technologically relevant electron acceptor (such as titanium dioxide) if the hot carriers have long lifetimes and the interface is properly controlled. This finding gives rise to insight on how to use hot carriers in highly-efficient CQDSCs. Sukhovatkin *et al.*⁵⁴ indirectly explored the MEG effects on both CQD solution and solid-state energetics through designing and fabricating a CQD-based photoconductive detector. By MEG effects, the internal gain of the photoconductive detector was found to dramatically enhance for photon energies greater than 2.7 times the quantum-confined bandgap. MEG effects have also been found in other colloidal nanoparticles including PbTe,⁵⁵ Si nanoparticles,⁵⁶ PbS CQDs,⁵⁷ PbSe,⁵⁸ CdSe,^{59,60} InAs,⁶¹ InP,⁶² and CdTe.⁶³

b. Improving interface quality. Today's state-of-the-art CQDSC efficiency is still not close to the S-Q limit; therefore the benefits of hot carriers or MEG have not been proven. The sharp increase of CQDSC efficiency in the last 8 to 9 years since the first certified CQDSC in 2010 can be ascribed to materials quality improvement. In other words, current state-of-the-art high-efficiency CQDSCs benefit from the improved CQD quality, the effective surface passivation process through the discovery and applications of various short-chain organic and inorganic ligands, from successful reduction of trap states in CQD/electrode (or metal oxide) interfaces, and better understanding of carrier transport dynamics in CQDSCs.

There are three types of interfaces in a CQDSC, i.e., CQD surface and/or CQD-CQD interface, CQD thin film/metal electrode, and CQD thin film/metal oxide interface. CQD surface passivation using organic dithiol ligand exchange⁶⁴ and inorganic atomic halide ligand⁶⁵ exchange are effective approaches for the removal of surface traps; therefore, they simultaneously remove midgap electronic states, thereby leading to increased V_{oc} .⁶⁶ To suppress CQD thin film/metal electrode interface induced radiative and nonradiative recombinations, the strategy of *energy band alignment* can be used. Bawendi *et al.*⁶⁷ introduced an EDT-passivated PbS CQD layer between the TBAI-passivated PbS CQD layer and the metal electrode, to adjust the energy band alignment by avoiding abrupt energy band bending at the CQD thin film/metal electrode interface. This approach successfully yielded certified efficiencies as high as 8.55% in 2014. Surface passivation of metal oxide nanostructures has also been demonstrated as an effective method to reduce CQD thin film/metal oxide interface-associated carrier recombinations. Kim *et al.*⁶⁸ reported high certified efficiency of 10.7% for ZnO/PbS CQD heterojunction solar cell through depositing robust self-assembled monolayers on nanostructured ZnO surface for improved interface energy alignment.

The best reported CQDSCs [Fig. 12(a)] with a planar heterojunction structure and certified efficiency of 11.28% is an example of CQDSC efficiency improvement through removing interface defects and/or CQD material quality. Figure 12(b) shows the tail states of CQD thin films in CQDSCs. These tail states can be introduced by CQD synthetic polydispersity and inhomogeneous aggregation during the ligand-exchange process. As shown in Fig. 12(b), the photoexcited excitons thermalize quickly upon generation and decay to the band edge. The existence of tail states causes carriers to flow into those band tail states to form an effective energy bandgap E'_g , which leads to reduced V_{oc} . Furthermore, when the tail states are deeper than the ZnO conduction band energy, carrier injection into the ZnO is hindered, which causes a decreased J_{sc} . However, band tail states can be removed or reduced through a solution-phase ligand-exchange process, which results in high CQD thin film quality with flat energy configuration and advantageous highly packing density. With the removal or reduction of tail states, both V_{oc} and carrier injection can be improved.

Therefore, as can be concluded from the above discussion involving CQD materials and solar cells, the efficiency improvement of current state-of-the-art CQDSC is driven by the improvement of CQD quality, chemical processing, and ligand passivation. The theoretical efficiency of ~44% for CQD solar cells, which is much higher than that of Si-based solar cells, is attributed mainly to the wider light absorption spectral range and the multiple

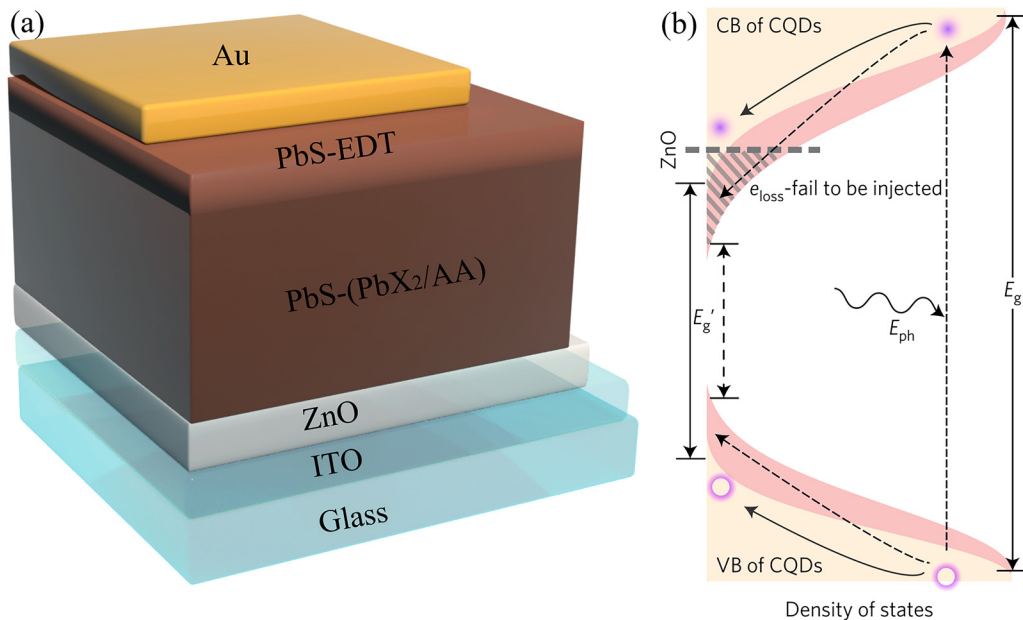


FIG. 12. (a) Schematic of the sandwich structure of CQDSCs certified with the PCE as high as 11.28%, the highest reported efficiency to date. (b) Illumination of tail state effects on solar device V_{oc} and injection efficiency of carriers. Thermalized carriers flow to the tail states formed at the ZnO/CQD thin film interface; they result in a V_{oc} deficit and an effective bandgap E_g' . When the tail states are deeper than the ZnO conduction band, carrier injection into the ZnO is not hindered. Effective reduction or removal of these tail states contributes to the increase of V_{oc} and J_{sc} as more carriers are injected into the electrode. EDT: 1,2-ethanedithiol. AA: ammonium acetate. PbX₂: lead halide. Reproduced with permission from Liu *et al.*, Nat. Mater. **16**, 258–263 (2017). Copyright 2017 Nature Publishing Group.

exciton generation effects when compared with its Si counterpart. However, the current highest experimental power conversion efficiency reported for CQD solar cells is no more than 17%,¹ which is due to limitations generated by defects in the CQDs themselves and in the surface passivation materials (dot-linking ligands). These defects create different carrier recombination channels and lead to a much smaller efficiency than the theoretical prediction. As a result, improving CQD material quality has been driving intensive research efforts.

II. CARRIER TRANSPORT CHARACTERIZATION TECHNIQUES FOR CQD MATERIALS AND SOLAR CELLS

A. Short-circuit current/open-circuit voltage decay (SCCD/OCVD)

SCCD and OCVD are two valuable techniques for measuring carrier lifetimes in CQD solar cells.⁶⁹ These techniques probe *pn* junction voltage and short-circuit current decay following the photoexcitation of electron-hole pairs to measure carrier recombination lifetimes.^{70,71} Unlike most techniques that can characterize only one carrier transport parameter, the combination of SCCD and OCVD can measure both the carrier lifetime, τ_r , and the back-surface recombination velocity, s_r , of a solar cell. The theoretical model is derived from the analysis of minority carrier diffusion within a *pn* junction, and the solar cell back-surface is treated

through boundary conditions. The differential equation for minority carrier concentration in the solar cell base can be expressed by

$$\frac{\partial \Delta n(x, t)}{\partial t} = D \frac{\partial^2 \Delta n(x, t)}{\partial x^2} - \frac{\Delta n(x, t)}{\tau_r} + G(x, t), \quad (10)$$

where $\Delta n(x, t)$ is the excess minority carrier density, D is the carrier diffusivity, and $G(x, t)$ is the generation rate which equals zero after the photoexcitation is turned off. The solution to Eq. (10) is subject to the following boundary equations:⁷¹

$$\frac{1}{\Delta n(x, t)} \frac{\partial \Delta n(x, t)}{\partial x} = - \frac{s_r}{D_n} \text{ for } x = d, \quad (11)$$

with

$$\Delta n(0, t) = 0 \quad (12)$$

for the short-circuit current method, and

$$\frac{\partial \Delta n(x, t)}{\partial x} = 0 \text{ for } x = 0 \quad (13)$$

for the open-circuit voltage method. d stands for the device thickness. When considering the above boundary conditions, the solution to Eq. (10) exhibits an exponential short-circuit current and open-circuit voltage decay profile with time. The decay behavior

has a time constant that is determined by the time-dependent excess carrier density.

For the open-circuit voltage decay method, generally, researchers calculate the minority carrier lifetime through^{69,72}

$$\tau_r = -\frac{FkT/q}{dV(t)/dt}, \quad (14)$$

with k being the Boltzmann constant, T the absolute temperature, q the elementary charge, and F a constant ranging between 1 at low carrier injection levels, and 2 at high carrier injection levels. Therefore, using the open-circuit voltage decay curve, the carrier lifetime can be resolved. Figure 13 shows a typical curve of V_{oc} decay and the best fit to Eq. (14) for the extraction of the minority carrier lifetime. Minority carrier lifetimes extracted using this method for PbS CQD solar cells in a Schottky architecture range from 1 ms at low intensities to 10 μ s at high intensities. In comparison, typical carrier lifetimes from several hundred nanoseconds to several milliseconds for Si-based photodiode are very common.

The disadvantages of the SCCD and OCVD techniques can be summarized as follows: first, these techniques need to make contact with solar cell devices. Measurements through contact with samples are time-consuming and can induce damage to the device. Second, SCCD and OCVD are based on the theoretical model as presented in Eqs. (10) and (14); therefore, it is evident that only effective carrier lifetimes can be measured and these techniques cannot distinguish bulk and surface lifetimes. Although the back-

surface recombination velocity is introduced through boundary conditions, the front surface recombination velocity is not measured. Third, these techniques cannot detect depth-resolved carrier transport parameters as the signals of SCCD and OCVD are from the overall short-circuit current and open-circuit voltage of the device, which is contributed by carriers at different depths. Fourth, these techniques can only be used for complete solar cells and they do not apply to semiconductor wafers or incomplete photovoltaic devices, which have no short-circuit currents and open-circuit voltages.

B. Photoconductance decay (PCD)

PCD has been the best-developed technique for semiconductor lifetime characterization since 1955 when it was proposed for the first time. With a principle directly based on the definition of carrier lifetime, this technique can measure carrier lifetime with high accuracy and reliability. In PCD, electron-hole pairs are generated through pulsed photoexcitation and their time-dependent concentration decay is monitored with respect to time following the cessation of the photoexcitation. The sample is in contact with an electrical circuit for PCD measurements, but the method can also be contactless if microwaves are used in reflection or transmission mode, and this variant has been named microwave photoconductivity (μ -PCD).^{73,74} For μ -PCD, photoconductivity is monitored through microwave reflection or transmission changes due to absorption by free carriers.

The theory of PCD starts with the expression for conductivity σ ,

$$\sigma = q(\mu_n n + \mu_p p), \quad (15)$$

where q is the elementary charge and n and p are the electron and hole concentrations, respectively. The terms $\mu_{n,p}$ represent the electron (n) or hole (p) mobility, respectively. Furthermore, $n = n_0 + \Delta n$ and $p = p_0 + \Delta p$ (n_0 and p_0 are electron and hole concentrations at equilibrium, respectively). Assuming identical electron and hole mobilities, at low injection levels, the excess carrier concentration is much lower than the carrier concentration at equilibrium. For low trapping conditions, i.e., $\Delta n = \Delta p$, a measurement of conductivity change corresponds to the measurement of excess carrier changes, which are given by

$$\Delta n = \frac{\Delta \sigma}{q(\mu_n + \mu_p)}. \quad (16)$$

Therefore, assuming constant mobilities, the measurement of Δn can be carried through measuring $\Delta \sigma$. For the calculation of carrier lifetimes, the dependence of carrier concentration decay on time is determined by the carrier lifetime τ through⁷⁵

$$\Delta n(t) = \Delta n(0) \exp\left(-\frac{t}{\tau}\right). \quad (17)$$

PCD measures an effective minority carrier lifetime, τ_{eff} and cannot distinguish bulk lifetime, τ_B , and surface lifetime, τ_s ; in other words, τ in Eq. (17) is an effective carrier lifetime τ_{eff} that

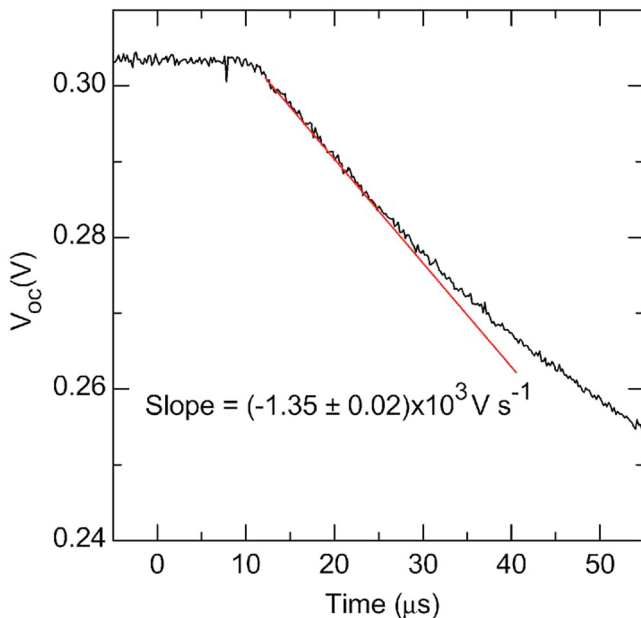


FIG. 13. Typical open-circuit voltage decay curve for CQD solar cells: the linear best fit (dashed red line) is used for the determination of recombination-determined carrier lifetime. Reproduced with permission from Johnston *et al.*, Appl. Phys. Lett. **92**(12), 122111 (2008). Copyright 2008 AIP Publishing LLC.

can be expressed as

$$\frac{1}{\tau_{eff}} = \frac{1}{\tau_B} + \frac{1}{\tau_s}. \quad (18)$$

This implies that if either bulk or surface lifetime is of interest, the other carrier lifetime must already be known.

Crisp *et al.*⁷⁶ applied contactless, time-resolved microwave conductance measurements to study charge transport in films of InP and InZnP CQDs that are linked with various short ligands such as $(NH_4)_2S$, Na_2S , EDT (palmitate, ethanedithiol), and PA (palmitate). It was found that transport in InP QDs is dominated by trapping effects, and with the help of PCD, charge carrier mobilities and lifetimes have been improved through ligand-exchange treatments for device-grade quality CQD thin film materials. An example of measuring the carrier mobility of InP CQDs using PCD is shown in Fig. 14. The CQDs were treated with $(NH_4)_2S$. Through fitting the PCD signal to a theoretical model, the carrier mobilities were obtained for CQDs for different photon fluences. Additionally, a half-life of ~ 30 ns for $(NH_4)_2S$ -capped CQDs was also determined with this method.

PCD has several significant disadvantages. (1) The instrumentation system of PCD is relatively complex. For the contactless mode μ -PCD, two systems, including the photoexcitation and the microwave conductance testing component, must be implemented. In comparison, other techniques, such as photothermal beam

deflection (PBD), transient PL, photocarrier radiometry (PCR), and heterodyne lock-in carrierography (HeLIC), only require a photo-excitation system while retaining the all-optical, contactless, and non-destructive character. (2) As discussed above, the PCD equations (17) and (18) describe effective carrier lifetimes originating from the combined effects of bulk and surface lifetimes (the latter in the form of surface recombination velocities) and carrier diffusivity. Specifically, μ -PCD cannot distinguish these parameters, although PCD has this capability through electrical contact with the sample, thereby compromising the all-optical, contactless, and non-destructive character. (3) PCD signals are depth-integrated along with the sample thickness; this implies that PCD is unable to depth resolve sample properties. The net effect of this feature is that, no matter how deep trap states lie, if they are within the carrier diffusion length, they can contribute to the detected PCD signal. In summary, for imaging applications, although μ -PCD can reveal image contrast, which originates from sample quality variations in different regions, it cannot determine whether these defects are on the surface, subsurface, p-n junctions, bulk, or even on the back surface. This is an important drawback and limitation in applications for the characterization of p-n junction based devices.

C. Time-resolved PL (TRPL, transient PL)

Photoluminescence (PL) techniques detect only radiative-recombination-induced photoemission. For example, depending on the specific semiconductor energy bandgap, the central photo-emission wavelength is $1.2\ \mu m$ for semiconductor Si. Therefore, InGaAs is the most commonly used material for PL detectors. PL based techniques can be further divided into steady-state and time-resolved PL (TRPL). The former can characterize semiconductor material optical and electrical properties including energy bandgap and trap states. Specifically, as reported in our previous publications,^{10,77} and shown in Fig. 15(a), PL spectra of two PbS-MAPbI₃-passivated PbS CQD thin films exhibit the dot size-dependent quantum dot bandgap energy, which is 1.1 eV and 1.0 eV for sample A (small dots) and B (big dots). Additionally, in Fig. 15(a), sample A has a smaller FWHM (full width at half-maximum) than sample B, reflecting a narrower quantum dot size distribution, as the broadening of PL peaks arises from the quantum dot size polydispersity with specific spectral components originating from dots of specific sizes. Furthermore, 200-nm thick CQD thin films capped with different ligands have also been characterized by steady-state PL. As shown in Fig. 15(b), three CQD thin film samples capped with MAPbI₃ (PbS-MAPbI₃ in the figure legend), EDT (PbS-EDT) and TBAI(PbS-TBAI) have the same band-to-band energy gap of 1.21 eV. To compare, PbS-MAPbI₃-B also passivated with MAPbI₃ while having a bigger quantum dot size, when compared with PbS-MAPbI₃, shows a bandgap energy red-shift to 1.09 eV, in agreement with Fig. 15(a). In addition, secondary PL emission peaks are also characterized both in Figs. 15(a) and 15(b), such as those at 0.81 eV (PbS-MAPbI₃) and 0.83 eV (PbS-TBAI), as well as the PL shoulder at 0.99 eV (PbS-EDT). These secondary PL emission peaks originate from recombinations that occur through defect-induced donors/acceptors arising from unpassivated surface states, structural defects, or other changes induced during ligand-exchange processes.

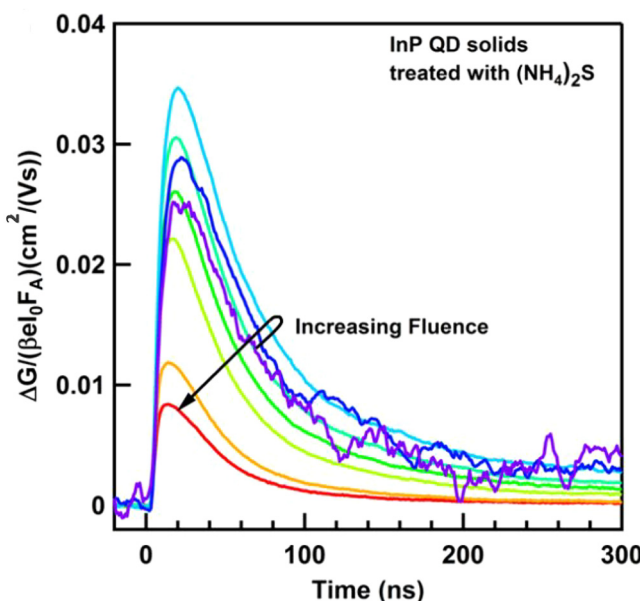


FIG. 14. Time-resolved microwave conductance measurement of InP QD solids treated with $(NH_4)_2S$. The y axis displays the mobility obtained by fitting the detector signal to a theoretical model. The measurement shows a half-life of ~ 30 ns for $(NH_4)_2S$ -capped QDs. Fluence here refers to the absorbed photon fluence. Reproduced with permission from Crisp *et al.*, ACS Appl. Energy Mater. 1(11), 6569–6576 (2018). Copyright 2018 American Chemical Society.

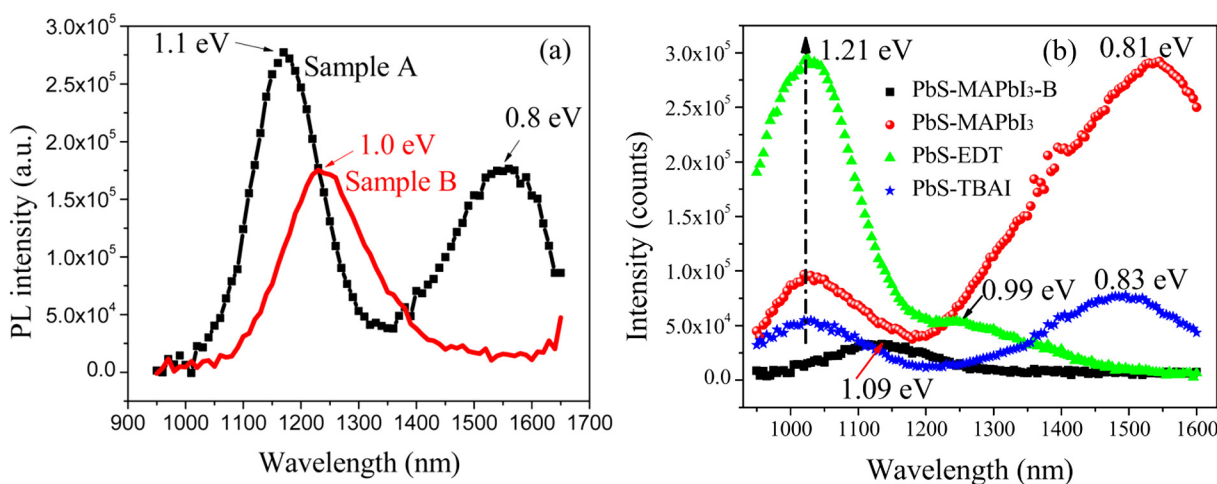


FIG. 15. (a) PL spectra of PbS-MAPbI₃-passivated PbS CQD thin film spin-coated on glass substrates. Sample A has a smaller quantum dot size when compared with Sample B. Reproduced with permission from Hu *et al.*, J. Phys. Chem. C **120**(26), 14416–14427 (2016). Copyright 2016 American Chemical Society. (b) PL spectra of four PbS CQD thin films with surface passivated with MAPbI₃, EDT, and TBAI. The legend PbS-MAPbI₃-B refers to MAPbI₃-passivated CQDs with a bigger quantum dot size than the other three samples: PbS-MAPbI₃, PbS-EDT, and PbS-TBAI. PbS-MAPbI₃, PbS-EDT, and PbS-TBAI have the same quantum dot size. Reproduced with permission from Hu *et al.*, Sol. Energy Mater. Sol. Cells **164**, 135–145 (2017). Copyright 2017 Elsevier B.V.

In comparison, TRPL is capable of measuring carrier lifetimes, back and front recombination velocities, and diffusivity with proper theoretical models.

Concerning the TRPL spectra at different decay time ranges, a PL vs time curve may have different slopes that correspond to different carrier recombination mechanisms. Therefore, different TRPL theoretical models can be applied within specific decay time ranges for the extraction of carrier lifetime and other transport parameters.^{78,79} As an example, a typical spectrum of TRPL is shown in Fig. 16. Upon the generation of excitons in PbS CQDs, these excitons diffuse through hopping or tunneling and dissociate into free electrons and holes as described in the inset of Fig. 16. Figure 16 reveals that there are two different carrier decay mechanisms of excitons and charge carriers in CQD thin films, i.e., the fast PL emission decay component that corresponds to the exciton dissociation process and the slow exponential decay component originated from free charge carrier trapping in CQD surface states.²³ The excess carrier decay in TRPL is also described by Eq. (17). The PL intensity is depth-integrated concerning excess carrier density along with the sample thickness, i.e.,

$$\Phi_{PL} = K \int_0^d \Delta n(x, t) dx, \quad (19)$$

where Φ_{PL} is the PL intensity, d is the sample thickness, and K is a constant. Therefore, the minority carrier lifetime can be extracted from fitting the exponential PL intensity decay profile to a single-exponential equation⁸⁰

$$\Phi_{PL}(t) \sim \exp(-t/\tau_{PL}). \quad (20)$$

Sometimes a multi-exponential decay model is used for better fitting and describing carrier decay mechanisms. The analytical model, however, can be very complicated depending on the carrier transport parameters that need to be extracted from a PL decay

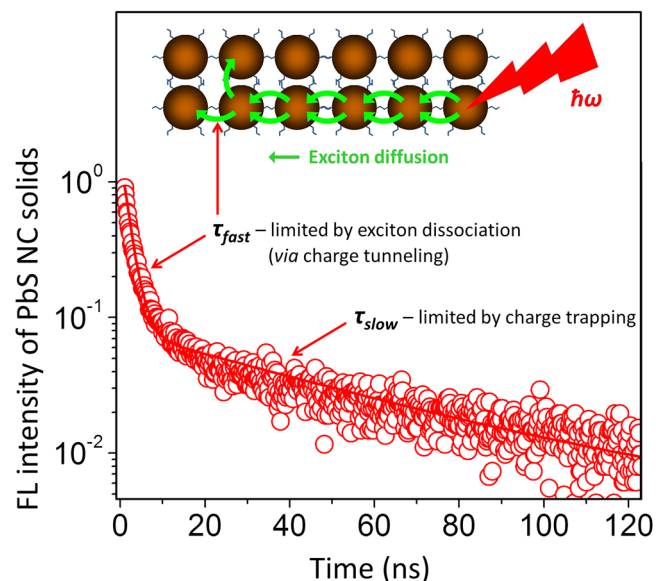


FIG. 16. A typical spectrum of time-resolved PL for PbS CQDs. The inset illustrates exciton transport through diffusion and dissociation. Reproduced with permission from Kholmicheva *et al.*, ACS Nano **9**(3), 2926–2937 (2015). Copyright 2015 American Chemical Society.

spectrum.⁷⁹ According to the foregoing discussion, transient PL measures the effective minority carrier lifetime. For example, when self-absorption is considered as a source of extra electron–hole-pair excitation (the influence of self-absorption is more significant for direct bandgap semiconductors such as PbS), the PL lifetime is defined as⁸¹

$$\frac{1}{\tau_{PL}} = \frac{1}{\tau_{non-rad}} + \frac{1}{\tau_S} + \frac{1}{\gamma\tau_{rad}}, \quad (21)$$

where the terms $\tau_{non-rad}$, τ_S , and $\gamma\tau_{rad}$ are the nonradiative, surface, and radiative lifetimes, respectively, and the term γ denotes the photon recycling factor. However, the effect of self-absorption is not substantial for indirect bandgap semiconductors.

In recent years, InGaAs camera-based PL imaging of semiconductor materials and devices has emerged. Transient PL has many advantages, for example, it directly measures carrier radiative recombination without influence from thermal infrared photon emission, which can simplify theoretical computations. Besides, near-infrared InGaAs cameras or single-element detectors do not need cooling, which eases requirements for the testing environment and improves measurement accuracy. Currently, with increases in InGaAs camera frame rates, fast carrier transport property characterization has become possible. Nevertheless, transient PL has several disadvantages which can be summarized as follows: (1) The absence of a narrow bandpass noise filtering interface such as a lock-in amplifier renders transient PL of materials and devices with fast lifetimes inapplicable or inaccurate due to low signal-to-noise ratio (SNR). Besides, experimental system calibration is required.⁸⁰ (2) The PL signal is depth-integrated along with the sample thickness, which makes it impractical to distinguish carrier transport properties at different depths, thereby limiting applications to photovoltaic device characterization. (3) Although transient PL can measure multiple carrier transport parameters, this technique is still constrained by low state-of-the-art camera frame rates and the requirement for long exposure time to attain measurable SNR.

D. Photocarrier radiometry (PCR)

Photocarrier radiometry (PCR) is a dynamic frequency-domain PL method that collects radiative recombination events within semiconductor materials. This technique evolved from photothermal radiometry (PTR) that collects signals from non-radiative recombination, i.e., PCR is complementary to PTR in the sense that it is only sensitive to radiative recombinations and emissions.^{82,83,85} More specifically, PCR is spectrally gated to filter out thermal infrared photon emissions from semiconductors, thereby measuring optoelectronic transport properties in materials and devices without superposition and interference of thermal processes such as hot carrier decay and lattice absorption, which, however, will be collected as signal in PTR systems. PCR uses modulated lasers to excite semiconductor samples. The lock-in-amplifier-demodulated near-infrared radiation signals can quantitatively measure carrier transport parameters. In comparison with photothermal techniques, i.e., PTR and its imaging evolution lock-in thermography (LIT), which detect both thermal waves and carrier density waves, the theoretical interpretation of PCR signal is much easier with fewer unknown parameters involved, corresponding to relatively higher measurement accuracy. For this

reason, the use of PCR has grown in recent years in the optoelectronic materials community. The close relationship between PTR and PCR, and between their respectively corresponding imaging evolutions LIT and HoLIC/HeLIC (homodyne lock-in carrierography and heterodyne lock-in carrierography), can be used as complementary modalities toward a better understanding of PCR signals and LIC images. Therefore, PTR and LIT will be presented briefly in the beginning of this section by showing how they are used for studying Si-based materials and devices.

1. Photothermal radiometry (PTR) and lock-in thermography (LIT)

PTR and LIT are two major techniques that have been investigated intensively and are under rapid improvement for semiconductor diagnostic applications.^{84–87} Nowadays, these techniques are among the most advanced and mature methods for full photothermal nondestructive characterization of semiconductor materials and devices. LIT is the camera-based imaging extension of PTR, which uses a single detector for signal collection.

However, the dynamic range of this kind of imaging has been limited by the relatively low camera frame rates and exposure times as PL imaging is performed in the steady-state⁸⁸ or at low modulation frequencies⁸⁹ and thus it cannot operate at high modulation frequencies required for fast carrier transport characterization. Figure 17(a) shows a schematic of PL imaging for a quasi-steady-state model in which four images were recorded at a low-frequency-modulated square wave excitation. The effective minority carrier lifetime could be measured by fitting each pixel of these images to a time-domain theoretical model. Similarly, Fig. 17(b) presents the mechanism used for PL imaging at low modulation frequencies. Low-frequency-modulated PL imaging can also yield effective minority carrier lifetime images from proper frequency domain theoretical models.

In PTR, modulated photoexcitation with superbandgap energies is applied to the semiconductor surface which generates electron–hole pairs, followed by radiative and nonradiative recombination processes. Energy from non-radiative recombination is emitted through the form of heat (radiative heat transfer) in the mid-infrared range between $5\text{ }\mu\text{m}$ and $12\text{ }\mu\text{m}$, depending on the temperature rise and energy levels of trap states in a semiconductor.⁸⁸ One of the major advantages of PTR and LIT is the high SNR due to lock-in amplifier detection. Also, the presence of two independent amplitude and phase channels enhances the measurement uniqueness and reliability. Figure 18 shows a typical LIT experimental setup. By fitting a series of experimental amplitude and/or phase signal responses in a wide range of frequencies to suitable theoretical models, as shown in Fig. 19, multiple carrier transport parameters can be obtained such as recombination lifetime, diffusivity, and front and back-surface recombination velocities (SRVs).

The emergence of mid-infrared charge-coupled devices (CCDs) has enabled the realization of large-area LIT imaging. Compared with static PL and EL imaging techniques, LIT has higher SNR values that lead to high image quality. LIT is sensitive to trap and defect states as these states can produce intensified heat emission (large signals) through enhanced non-radiative recombinations. The major advantage of dynamic imaging like LIT is the

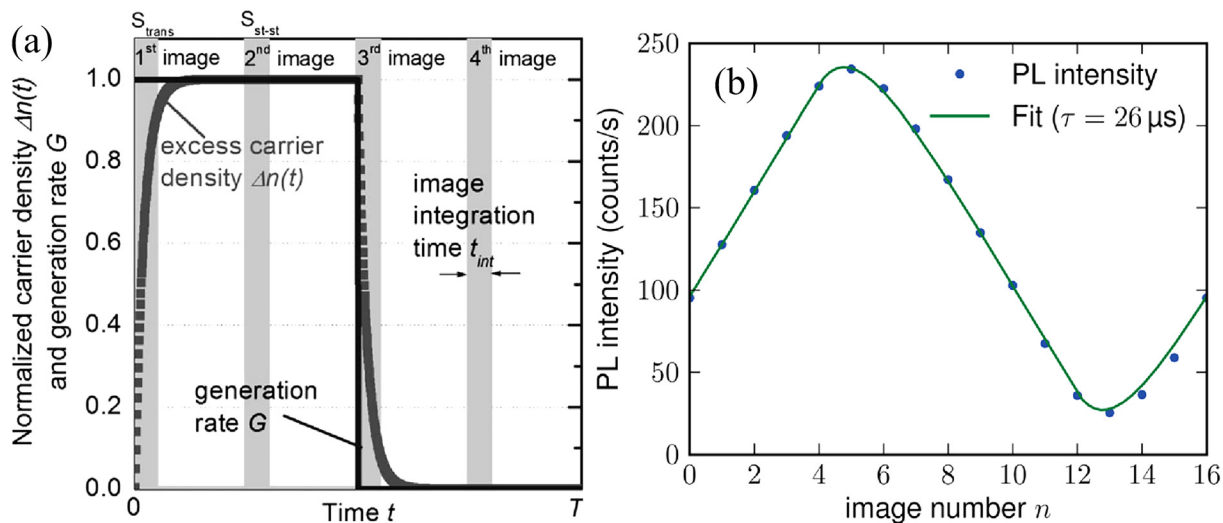


FIG. 17. The mechanism for quasi-static PL imaging (a). Reproduced with permission from Ramspeck *et al.*, J. Appl. Phys. **106**(11), 114506 (2009). Copyright 2009 AIP Publishing LLC. (b) The mechanism for low-frequency-modulated PL imaging. Reproduced with permission from Kiliani *et al.*, Appl. Phys. Lett. **110**(5), 054508 (2011). Copyright 2011 AIP Publishing LLC.

enhanced image contrast compared to static (dc) camera imaging. The disadvantages of LIT can be summarized as follows: (1) Low resolution. For thermal emission-based techniques, image resolution is determined by the thermal diffusion length which, however, is generally as long as several millimeters at low modulated excitation frequencies in high-quality semiconductors with long recombination lifetimes and high carrier diffusivities.⁹¹ Although the thermal diffusion length can be reduced by increasing modulation frequency, the SNR is simultaneously reduced, which decreases image quality and contrast. (2) Low SNR due to the image-capturing CMOS mid-infrared cameras. High background (dc) temperature raises the camera baseline, which can lead to image deterioration and ultimate saturation. Therefore, the thermal environment must be meticulously controlled to reduce thermal noise from the surroundings to achieve high image quality. (3) The complicated and intertwined mechanisms of thermal sources. Although the purpose of LIT and PTR is to study excess carrier dynamics, the collected signals are thermal in nature and they result from three main mechanisms all of which synchronously contribute to the modulated semiconductor sample response: photon lattice absorption, hot carrier thermalization, and carrier non-radiative recombination. To measure device-relevant transport parameters, very complicated theoretical and computational procedures are needed that lead to reduced measurement reliability and uniqueness, as well as increased testing time. (4) Similar to μ -PCD, LIT can only detect effective carrier lifetime. This is due to the low frame rate of mid-infrared cameras that limit LIT imaging to relatively low frequencies (<1000 Hz). As a result, the low modulation frequencies used in PTR and LIT cannot detect fast carrier transport behavior, which is characteristic of transport phenomena in CQD materials and devices. Therefore, PCR-based techniques, aiming to resolve fast carrier transport parameters, are invented as detailed in Secs. II D 2 and II D 3.

2. Photocarrier radiometry instrumentation

As a non-destructive, frequency-domain, spectrally gated PL technique, PCR uses a superbandgap frequency-modulated laser beam to create a periodic carrier density wave (CDW) in semiconductor

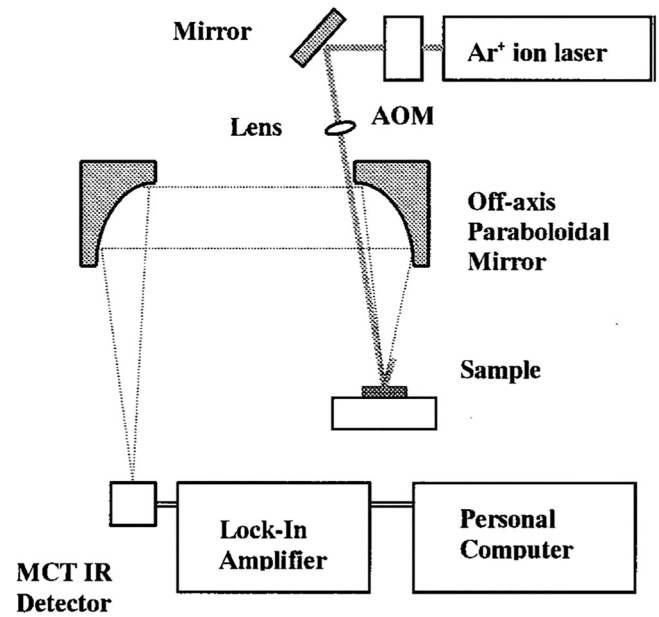


FIG. 18. Schematic of the experimental setup for photothermal radiometry (PTR).⁹⁰ Reproduced with permission from Ikari *et al.*, J. Appl. Phys. **85**(10), 7392–7397 (1999). Copyright 1999 AIP Publishing LLC.

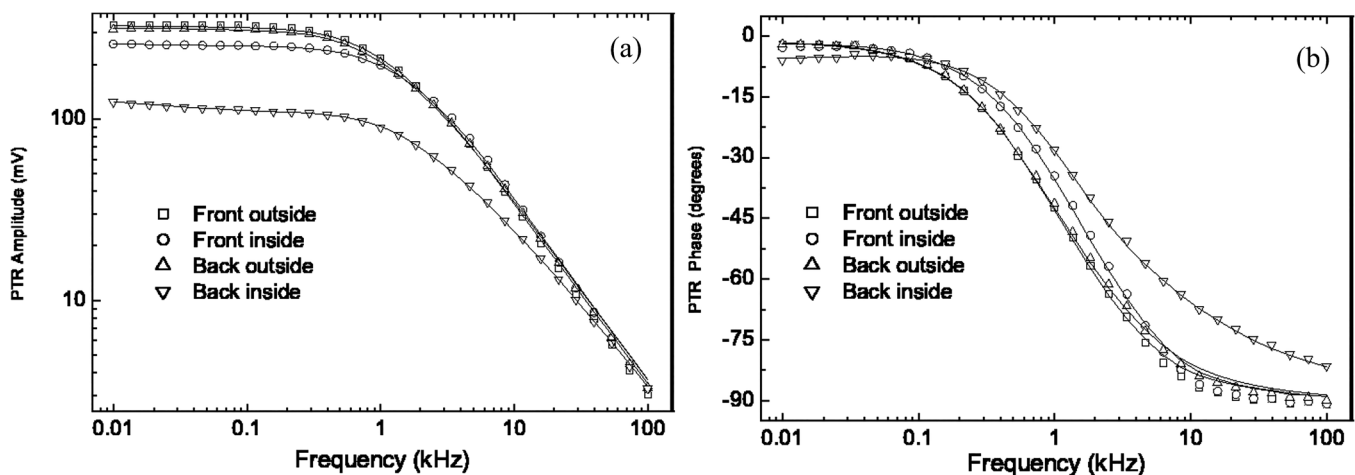


FIG. 19. Representative experimental frequency-dependent amplitude (a) and phase (b) for a p-Si wafer. Front and back indicate signals obtained with the laser illuminating the front and back surface of the wafer; outside and inside refer to the coordinates of a defect area. The continuous lines are best fits to PTR theory that generate multiple carrier transport parameters including carrier lifetime, diffusivity, and surface recombination velocities. Reproduced with permission from Mandelis *et al.*, Phys. Rev. B 67(20), 205208 (2003). Copyright 2003 American Physical Society.

materials and devices. The amplitude and phase of the periodic signal are demodulated using a lock-in amplifier. PCR amplitudes and phases span from low frequencies ($\omega\tau \ll 1$, in which ω is the modulation angular frequency and τ is the effective carrier lifetime) to high frequencies ($\omega\tau \gg 1$) and can be used for fitting theoretical models to data to extract useful carrier transport parameters. The PCR instrumentation consists of four key subsystems as shown in Fig. 20:

1. excitation laser generation system,
2. dynamic photoluminescence detection system,
3. lock-in amplifier signal demodulation system, and
4. a computer interface to perform the data analysis and parameter extraction.

The excitation laser generation system consists of a function generator, a laser, and other optics including various mirrors as shown in Fig. 20. A typical function generator for PCR detection is from Stanford research systems, Model DS340, synthesized function generator. A typical PCR system for CQD materials and device characterization uses a near-infrared diode laser with DC power ~ 30 mW. Laser power is modulated sinusoidally from 10 Hz up to several MHz with an accuracy of ± 25 ppm determined by the function generator.

The PCR photonic emissions from the photoexcited semiconductor are collected by a single InGaAs detector (e.g., PDA400, ThorLabs), in front of which a long-pass filter (~ 1000 nm) is used to filter out the excitation laser. The PDA400 detector has a switchable gain for detecting light signals from DC to 10 MHz. The detector effective diameter is 1 mm with a spectral response from 800 nm to 1750 nm. For modulation frequencies from 10 Hz to 100 kHz, a typical gain is 30 dB. As shown in Fig. 20, the lock-in amplifier reference signal is sourced from the function generator,

and its input signal is the output of the InGaAs detector. The typical time constant τ for PCR measurement is 1 s.

3. General theory of photocarrier radiometry

PCR is an optical non-destructive dynamic spectrally gated frequency-domain PL modality. It is also an evolution of

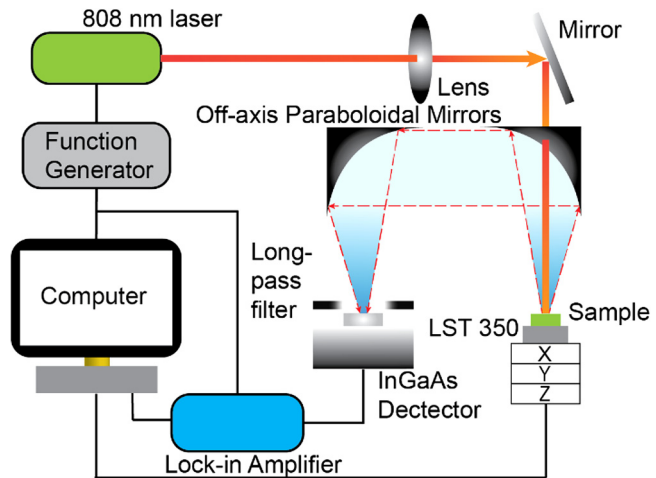


FIG. 20. Typical schematic of the experimental setup for photocarrier radiometry. Typical parameter settings from the function generator are output amplitude $10.96 V_{pp}$, indicating the peak-to-peak voltage of the sine wave, and DC offset 0.90 V. A general purpose interface bus (GPIB) interface is used for communication between the function generator and the computer. Reproduced with permission from Hu *et al.*, Sol. Energy Mater. Sol. Cells 174, 405–411 (2018). Copyright 2018 Elsevier B.V.

photothermal radiometry (PTR). PCR was developed⁹² as a purely carrier-wave laser-based detection methodology and eliminates the thermal-wave contributions. Because PCR is only sensitive to the recombination of photoexcited carrier density waves, its signal processing complexity and interpretation are much simpler than PTR, thereby increasing the uniqueness and reliability of the obtained semiconductor material properties. As the detailed theory has been presented elsewhere,⁸⁵ here, only some key conclusions will be discussed. Although the PCR theory was developed for the case of Si wafers, most concepts and formulas can be directly applied to other material systems such as GaAs⁹² and CQD thin films and solar cells.

PCR detects radiative photon emission from semiconducting and photovoltaic materials and devices. Therefore, the discussion of its theory should start with excess carrier recombination mechanisms. As shown in Fig. 21, electrons are excited by photons with superbandgap energy, then the excited electrons and holes quickly thermalize and relax to the band edge of the conduction and valence band, respectively, with the emission of phonons (or heat). De-excitation of photoexcited carriers occurs through three recombination mechanisms: radiative recombination, Auger recombination, and Shockley–Read–Hall (SRH) recombination. This is the fundamental physics behind PCR measurements, which yield radiative carrier kinetics and dynamics, and remains the same for both Si and CQD-based materials and devices. In other words, regardless of the continuous- or localized-band structure of a semiconductor (e.g., CQD or Si), the incident photon energy is always converted through one or more radiative, Auger, and non-radiative channels and also gives rise to external current generation in closed circuits. Therefore, the physics illustrated in Figs. 21 and 22 remains valid across all (opto)electronic materials. In other words, no matter which type of semiconductors (CQD or Si), the incident photon energy is always converted through one or more radiative, Auger, and non-radiative channels plus any external current generation in closed circuits. Therefore, the physics illustrated in Figs. 21 and 22 remains valid across all (opto)electronic materials. A detailed review of these recombination mechanisms can be found elsewhere^{93–95} and will be briefly described here.

Radiative recombination is a direct band edge electron-hole recombination, emitting photons with the bandgap energy of the semiconductor. As both electron and hole participate in the radiative recombination process, the recombination rate is proportional to the product of electron and hole concentrations. Auger recombination denotes direct non-radiative recombination of electrons and holes via energy transfer to, and emission of, another free carrier. It is a reverse process of MEG in QDs. Depending on whether the energy is transferred to an electron or hole, the three-particle interaction can be denoted by *eeh* or *ehh*. Auger recombination usually occurs under high carrier density conditions, the result of high injection levels. The recombination rate of an Auger is proportional to the product of the concentrations of the three particles involved. Shockley–Read–Hall recombination is a two-step process with carriers trapped into defect states and then followed by radiative and non-radiative recombination from these trapped states. The emitted photon energy of SRH recombination is lower than the semiconductor bandgap energy, depending on the energy levels of the involved defect states. SRH-associated defect states can be distinguished as

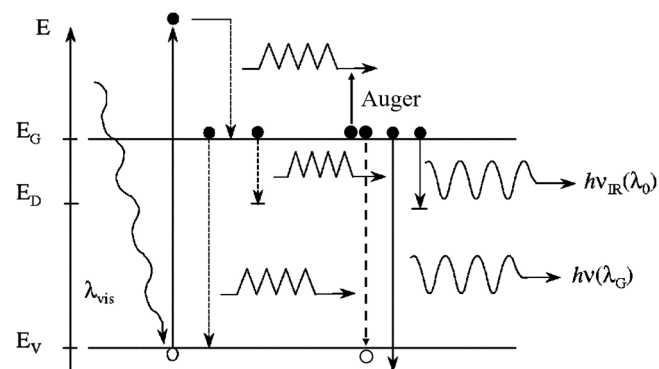


FIG. 21. (a) Energy diagram of an n-type semiconductor with the illumination of photoexcitation, and radiative and non-radiative recombinations. Defect related states are also depicted as participating in radiative and non-radiative recombinations. Reproduced with permission from Mandelis *et al.*, Phys. Rev. B **67**(20), 205208 (2003). Copyright 2003 American Physical Society.

recombination centers and traps. The capture coefficients of electrons and holes in recombination centers are similar. However, the capture coefficient for trapping one carrier is higher, while the rate for capturing another particle with the opposite sign for recombination is slow. It should be noted that SRH recombination not only can occur between defects and conduction/valence band but also between defect states. The recombination rate of SRH is

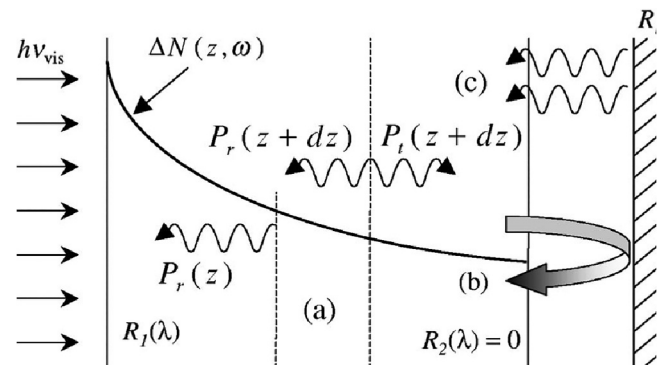


FIG. 22. Schematic of one-dimensional semiconductor materials (such as Si and CQDs) where radiative photon distribution emission follows laser excitation and carrier-wave generation. (a) A representative semi-conductor slab with thickness dz , centered at z . (b) Reflected photons from backing support material. (c) Emissive IR photons from backing support materials at temperature T_b . $\Delta N(z, \omega)$ represents the depth and frequency-dependent carrier diffusion wave, and L is the thickness of the semiconductor sample. Other parameters can be found in the text. $R_{1,2,b}(\lambda)$ stands for reflectivity at the front surface, the back surface, and the backing material, respectively. It should be noted that the backing material is used to support the sample but is not necessarily in contact with it.⁸⁵ Reproduced with permission from Mandelis *et al.*, Phys. Rev. B **67**(20), 205208 (2003). Copyright 2003 American Physical Society.

proportional to the product of free carrier concentration and trap state density.

For QDs with high surface-to-volume ratios, the surface (interface) trap related recombination is important and involves defect states. Therefore, it is a type of SRH recombination. However, the SRH theory is derived based on a single well-defined trap level, whereas semiconductor interfaces or surfaces arise due to the termination of crystal periodicity and induce a band of electronic states in the bandgap. This inconsistency requires an extended SRH recombination theory able to deal with the continuum of surface states across the semiconductor bandgap.⁹³

For CQD thin films and solar cells, the radiative recombination and radiative component of SRH recombination contribute to PCR, depending on the specific PL spectra of a sample as shown in Fig. 19.

The photoexcited carriers after ultrafast decay to the respective band edge diffuse within their statistical lifetime. If the excitation laser is intensity-modulated at a frequency $f = \omega/2\pi$ (ω is the angular frequency), the photogenerated carrier density constitutes a spatially damped CDW. The CDW oscillates diffusely away from its generation source due to its concentration gradient and recombines with a phase lag dependency on a delay time that equals the carrier statistical lifetime τ , a structure- and process-sensitive property. The schematic of photon excitation, absorption, and emission processes in semiconductor materials (such as Si and CQDs) is illustrated in Fig. 22. The one-dimensional geometry is suitable for thin semiconductor materials or for the case of using spread laser beams of large spot size. The emission photon power at wavelength λ with a bandwidth $d\lambda$ is given by⁸⁵

$$dP_j(z, t; \lambda) = \{W_{NR}[T_T(z, t); \lambda] + \eta_R W_{eR}(\lambda)\} d\lambda; \quad j = r, t, \quad (22)$$

where $W_{NR}[T_T(z, t); \lambda]$ is the non-radiative related power per unit wavelength, $W_{eR}(\lambda)$ is the radiative recombination generated photon power per wavelength, η_R is the quantum yield for radiative emission, $T_T(z, t)$ is the total temperature including the background temperature and the temperature increase following photon absorption and heat generation, and the subscript (r, t) denotes back-propagating (reflected) and forward-propagating (transmitted) power as shown in Fig. 20. The modulated superbandgap laser photons impinge on the front surface of the semiconductor and are absorbed within a short distance $[\alpha(\lambda)]^{-1}$ from the front surface, where $\alpha(\lambda)$ is the photon wavelength-dependent absorption coefficient. The emission spectra are within a broad wavelength range due to the various types of radiative recombination processes. The final PCR expression was derived in one dimension by Mandelis *et al.*⁸⁵ as a depth integral of the excess carrier density,

$$P(\omega) \approx F(\lambda_1, \lambda_2) \int_0^L N(z, \omega) dz. \quad (23)$$

The term $F(\lambda_1, \lambda_2)$ is an instrumentation coefficient which depends on the spectral emission bandwidth (λ_1, λ_2) , and the expression for $F(\lambda_1, \lambda_2)$ can be found in Ref. 85. The term ΔN is the excess free charge carrier density which depends on the material properties and carrier transport nature.

E. Homodyne (HoLIC) and high-frequency heterodyne (HeLIC) lock-in carrierography

HoLIC and HeLIC are the imaging evolution of PCR with the use of a CCD camera instead of a single-element detector.⁹⁶ Another difference, when compared with PCR, is that two laser excitation must be used when carrier relaxation rates are much higher than the camera frame rate. HoLIC can only construct low-frequency imaging while HeLIC can image semiconductor kinetic/dynamic processes at high frequencies. HeLIC can perform large-area, contactless, fast, all-optical, quantitative characterization of semiconductor materials and devices such as the case of QD substrates and devices. This section will discuss the HoLIC and HeLIC instrumentation and signal processing techniques and will address the nonlinear nature of HeLIC.

1. Instrumentation and signal processing techniques used in HoLIC and HeLIC imaging

Instead of using an InGaAs single-element detector, HeLIC uses high-speed a near-infrared InGaAs camera for signal collection as shown in Fig. 23. In the original HeLIC application, a suitable InGaAs camera (Goodrich SU320 KTSW-1.7RT/RS170) was used with the following features: 320×256 pixel active elements, the spectral bandwidth of $0.9\text{--}1.7\ \mu\text{m}$, 120 fps frame rate, and exposure times tuned between 0.13 and 16.6 ms.^{77,97} In comparison with PCR, two fiber-coupled diode lasers of 808 nm wavelength were used for optical illumination. For generating homogeneous illumination both laser beams were spread and homogenized using diffusers to generate a $10 \times 10\ \text{cm}^2$ square illumination area with small intensity variations (<5%). An optical long-pass filter (Spectrogon LP-1000 nm) was mounted in front of the InGaAs camera, resulting in an effective InGaAs camera bandwidth of $1\text{--}1.7\ \mu\text{m}$.

Due to the limitations of camera frame rate, a synchronous undersampling method was employed through the application of a data acquisition module (NI USB-6259), which produced a reference signal and an external trigger to the camera. Sixteen images per period were scanned with a frame grabber (NI PCI-1427) controlled through a homemade LabVIEW program. To understand undersampling, the Nyquist–Shannon sampling theorem is reviewed here:⁹⁸

“An analog signal with a bandwidth of f_a must be sampled at a rate of $f_s > 2f_a$ to avoid the loss of information,” where the term f_s is the sampling rate. When $f_s = 2f_a$ is satisfied, f_s is called the Nyquist rate. The theorem is a bridge connecting continuous-time (analog) signals and discrete-time (digital) signals. In HoLIC, if the sampling method is used, for a harmonic signal with frequency f , the sampling rate f_s should be greater than $2f$ to precisely acquire the signal information. Limited by the frame rate of 120 fps of the foregoing InGaAs camera, the highest frequency in HoLIC can be calculated to be 60 Hz. To ensure the imaging quality with sufficient exposure time (i.e., the maximum exposure time of 16.7 ms), HoLIC imaging at 10 Hz is generally performed. However, for most QD and other applications to electronic materials with short carrier lifetimes, the low-frequency ceiling (60 Hz) is not sufficiently high for high-frequency imaging as required to generate measurable phase lags. Therefore, an undersampling method must be used in HoLIC for higher frequency imaging. The undersampling method

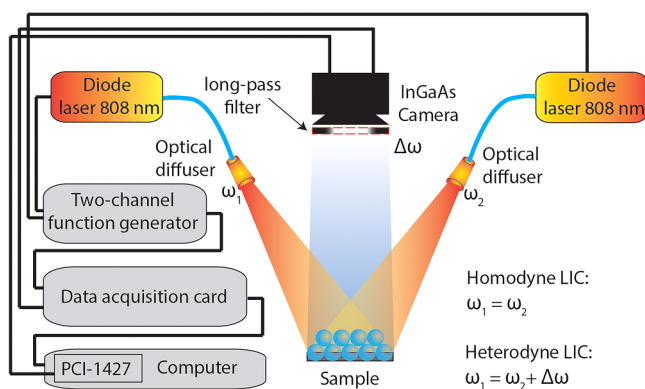


FIG. 23. Experimental setup for homodyne (HoLIC) and heterodyne (HeLIC) lock-in carrierography. Reproduced with permission from Hu *et al.*, Sol. Energy Mater. Sol. Cells **174**, 405–411 (2018). Copyright 2018 Elsevier B.V.

is also known as harmonic sampling, bandpass sampling, intermediate frequency (IF) sampling, and intermediate frequency (IF) to digital conversion. As shown in Fig. 24, considering a 1 Hz sine wave, 16 images are obtained in one period, a process known as oversampling. The process of taking 16 images per period (or 1 s, as shown in Fig. 24) corresponds to a frame rate of 16 Hz. If

undersampling is applied, skipping one waveform cycle, the actual frame rate used is only 1 Hz. Continuing in the same manner and skipping more waveform cycles, high-frequency imaging is achievable through the use of the highest frame rate. Given the known reference frequency, data using undersampling can be collected in a manner similar to oversampling as shown in Figs. 24(a) and 24(b). A complete schematic of HoLIC using the undersampling method is shown in Fig. 24(b), where one cycle is skipped between each image acquisition. For example, four images are obtained at 0, $\pi/2$, π , and $3\pi/2$ phases. The main pulse train plays the role of triggering the camera to start image acquisition, and the camera pulse train initiates four images (16 in real experiments) to be taken during a fixed camera exposure period. By skipping more cycles, higher modulation frequencies can be used while keeping the camera frame rate unchanged. The collected reference and signal data matrix is computed by use of a lock-in amplifier or data acquisition card shown in Fig. 23.

Despite the application of undersampling, problems still arise when high modulation frequencies are used. They include small timing errors and decreased resolution due to the limited camera exposure time; therefore, image distortion will occur. To overcome these issues, a heterodyne (HeLIC) method was introduced for high-frequency LIC imaging through the superposition of two modulated laser beams with a small frequency difference (the beat frequency) and the camera measuring with a frame rate equal to the beat frequency. The HeLIC experimental setup is the same as

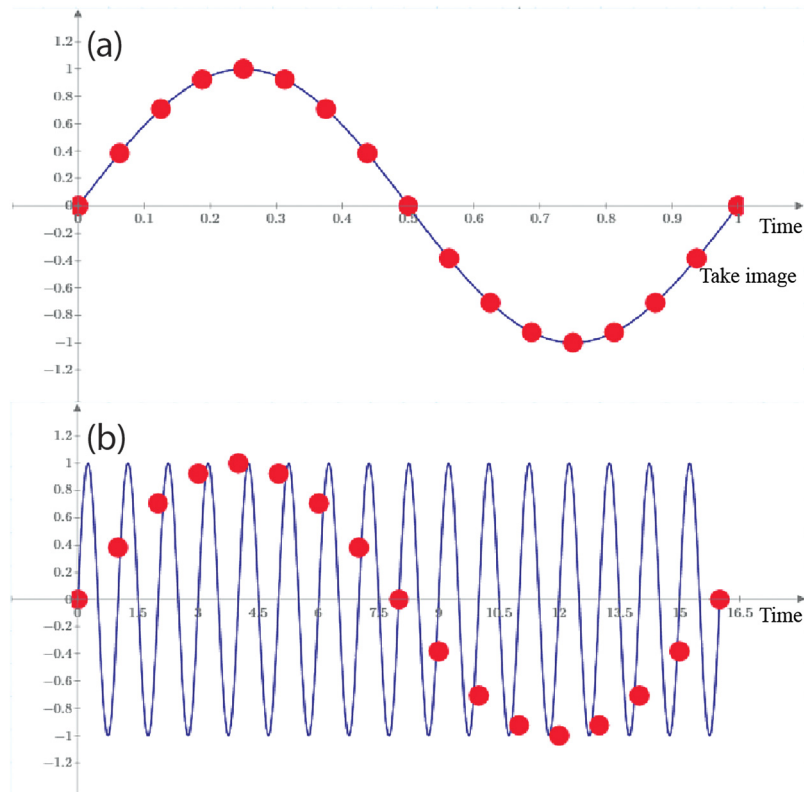


FIG. 24. Schematic of oversampling (a) and undersampling (b) signal processing methods. For sampling, 16 samples are taken per one cycle (waveform), and one circle (waveform) is skipped for undersampling.

that of HoLIC except that two laser excitations are modulated with a small frequency difference as shown in Fig. 23. Figure 25(b) displays the image generation mechanism of HeLIC imaging: The recorded image amplitudes carry information from the high modulation frequency due to the proximity of the two mixed frequencies f_1 and f_2 (Fig. 23). HeLIC imaging requires the nonlinear combination of two carrier density waves to create a carrier wave oscillating at the modulation frequency difference. Experimental evidence of the nonlinear response of CQD solar cells has been reported^{77,97} and a theoretical explanation of the nonlinearity is also discussed in this section with respect to analytical models. The physics behind the nonlinear response must be sought in the various carrier recombination mechanisms.

Given the fact that the photoexcited exciton population has a linear dependence on the incident photoexcitation intensity, for HeLIC imaging, the photoexcitation laser beam is modulated at two closely spaced angular frequencies (ω_1, ω_2), leading to the generation of two CDWs with a small frequency difference $\Delta\omega$ (which satisfies the relation $(\omega_1, \omega_2) \gg \Delta\omega$) mixed in a nonlinear

signal processing device, a mixer, such as a diode and a transistor.⁹⁹ The mixer creates a series of CDWs with new frequencies including $\Delta\omega$. For CQD solar cells, the sample itself acts as a mixer. The nonlinear coefficient γ of CQDs as a mixer can be obtained as shown in Fig. 26(a), through fitting the experimental DC image signal vs laser photoexcitation intensity to $I \propto N^\gamma$, in which I is the average amplitude of all image pixels and N is the excitation laser power density. A nonlinear coefficient γ of 0.60 was extracted consistently with the requirement for a non-linear process, $\gamma \neq 1$, to generate a HeLIC signal.^{77,97}

Theoretically, in HeLIC, as the laser excitation is modulated at two frequencies with an angular frequency difference $\Delta\omega$, the excess photocarrier wave can be expressed as

$$\begin{aligned} \Delta N(x, \omega) = & 2n_0(x) + A(x, \omega_1)\cos[\omega_1 t + \varphi(x, \omega_1)] \\ & + A(x, \omega_2)\cos[\omega_2 t + \varphi(x, \omega_2)], \end{aligned} \quad (24)$$

where $n_0(x)$ is the DC component of the modulated excess CDW, $A(x, \omega_j)$ is the amplitude of the cosinusoidally modulated CDW at

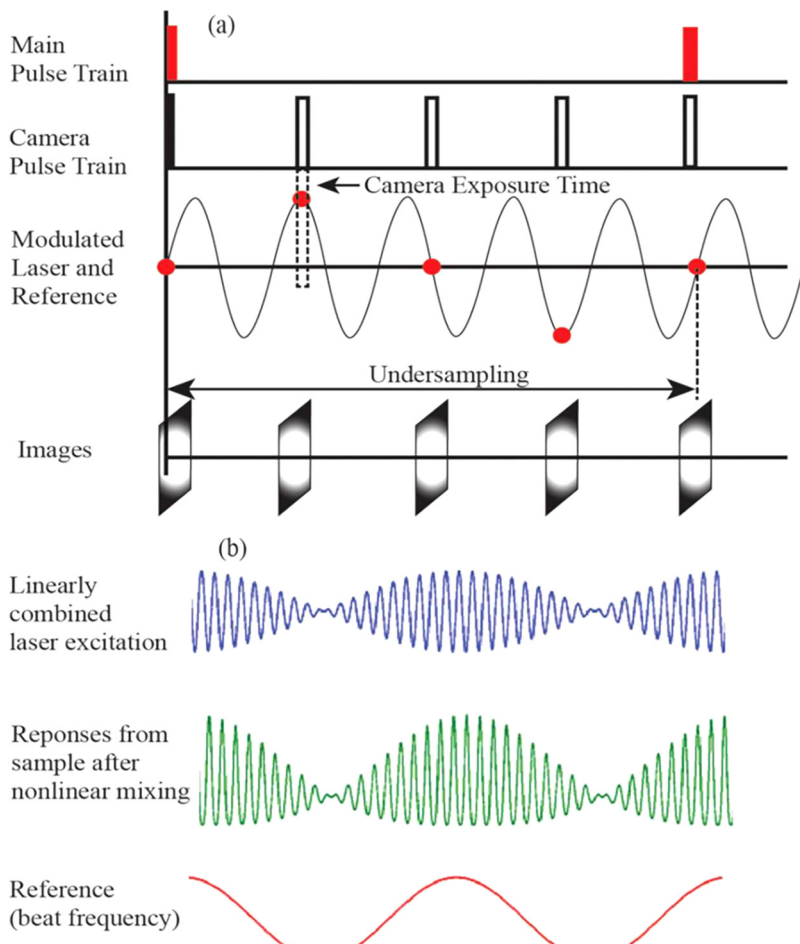


FIG. 25. Schematic of camera-based HeLIC imaging using an undersampling method (a). Modulation laser frequency mixing mechanism for HeLIC imaging (b). Reproduced with permission from Hu et al., J. Phys. Chem. C 120(26), 14416–14427 (2016). Copyright 2016 American Physical Society.

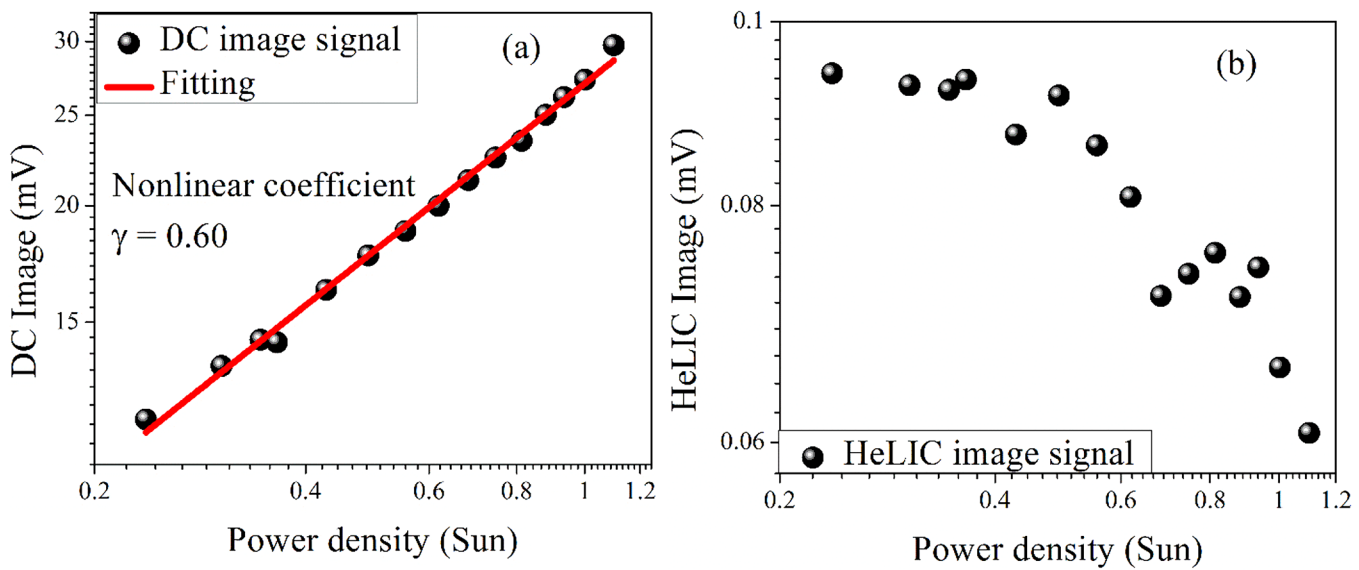


FIG. 26. The nonlinear dependence of DC (a) and HeLIC (b) signals on photoexcitation laser power density for our CQD solar cells with a typical structure: Au/PbS-EDT/PbS-PbX₂(AA)/ZnO/ITO. EDT: 1,2-ethanedithiol.

ω_j ($j = 1, 2$) and φ is the CDW phase. Equation (24) is only approximate since the PL emission response to photoexcitation intensity is a fundamentally non-linear process with a non-linearity coefficient γ , which has been generally measured to be between 0.5 and 2. Inserting $\Delta N(x, \omega)$ in Eq. (24) into Eq. (23) and considering the fully nonlinear response, it can be shown that

$$S(\omega) = F \int_0^d [2n_0(x) + A(x, \omega_1)\cos[\omega_1 t + \varphi_1(x, \omega_1)] + A(x, \omega_2)\cos[\omega_2 t + \varphi_2(x, \omega_2)]]^\gamma dx. \quad (25)$$

Furthermore, the integrand can be expanded using the binomial theorem in the form

$$\begin{aligned} & \left\{ 2n_0(x) + A(x, \omega_1)\cos[\omega_1 t + \varphi_1(x, \omega_1)] + A(x, \omega_2)\cos[\omega_2 t + \varphi_2(x, \omega_2)] \right\}^\gamma \\ &= \sum_{k=0}^{+\infty} \binom{\gamma}{k} \sum_{m=0}^{+\infty} \binom{\gamma - k}{m} [2n_0(x)]^{\gamma - k - m} \{A(x, \omega_1)\cos[\omega_1 t + \varphi_1(x, \omega_1)]\}^m A(x, \omega_2)\cos[\omega_2 t + \varphi_2(x, \omega_2)] \end{aligned} \quad (26)$$

Equation (25) can be further expanded using $\cos^k(\omega t) = 2^{-k} \sum_{m=0}^{\infty} \binom{k}{m} e^{i(k-2m)\omega t}$. As only signals modulated at the beat frequency $\Delta\omega = |\omega_2 - \omega_1|$ contribute to HeLIC, the demodulated HeLIC signal can be finally written as

$$S(\Delta\omega) = F \sum_{m=0}^{+\infty} \sum_{n=0}^{+\infty} \frac{\prod_{l=0}^{2m+2n+1} (\gamma - l)}{4^{m+n} m! (m+1)! n! (n+1)!} \int_0^d \frac{1}{2} n_0(x)^\gamma \left[\frac{A(x, \omega_1)}{n_0(x)} \right]^{2m+1} \left[\frac{A(x, \omega_2)}{n_0(x)} \right]^{2n+1} e^{i\Delta\varphi(x)} dx. \quad (27)$$

In Fig. 24(b), the dependence of wideband (1–270 kHz) HeLIC images on the laser photoexcitation power was investigated using a fixed 1-sun average intensity of modulated spread excitation beam while changing the DC excitation intensity, i.e., $n_0(x)$ in Eq. (27) changed from 0.2 to 1.1 sun. It was found that the average amplitude of HeLIC images decreases with increasing DC photoexcitation intensity, which contrasts with its DC counterpart as shown in

Fig. 26(b). The decrease of the HeLIC signal with DC excitation is in agreement with Eq. (27) due to the decreasing overall dependence on $n_0(x)$: $n_0(x)^{\gamma - 2(m+n+2)}$; $\gamma = 0.6$, $m, n \geq 0$. For CQD systems with discrete energy bands induced by spatial and energy disorder, the photogenerated excitons cannot dissociate immediately into free charge carriers, in contrast to those generated in continuous energy band semiconductors such as Si. Therefore, without the assistance

of external forces including interdot coupling and material interface effects, excitons are the dominant energy carriers in CQD systems and act as the main radiative recombination sources.⁷⁷ Based on the dominance of exciton dynamics, it was reported that the coefficient $\gamma = 1$ for excitonic transitions while $\gamma = 0.5$ for carrier recombination induced by trap- or doping-associated states.⁷⁷ Hence, the physical meaning of Eq. (27) can be interpreted as an evolution of the well-known exponential relation between photoexcitation and PL, $I \propto N^\gamma$, in the HeLIC framework. In summary, the decreased HeLIC signal with increased DC photoexcitation intensity shown in Eq. (27) results from three physical facts: unoccupied trap state density increases through enhanced photon absorption-mediated carrier ejection, increased exciton density mediated carrier recombination, and the nature of radiative PL signal collection in a heterodyne mode.

Figures 27(a) and 27(b) present photos of MAPbI₃-passivated PbS thin films. The thin films were spin-coated on glass substrates with an area of 25 × 25 mm² and stored together in a nitrogen environment for further study. It is observed that these thin films are

visually homogeneous with few visible imperfections. From a series of CQD thin films with different QD sizes, we have experimentally observed that the CQD thin film color changes slightly with QD size. This is consistent with the expected change in quantum confinement, which affects the optical absorption coefficient of these quantum dots, thereby accounting for the slight color difference between Figs. 27(a) and 27(b). In contrast, homodyne and heterodyne LIC images shown in Figs. 27(c)–27(f) illustrate significant degrees of inhomogeneity. The physical origins of the LIC spatial contrast are due to the free photocarrier density diffusion-wave distributions, which depend on charge carrier transport parameters, mainly the effective exciton lifetime as well as the hopping diffusivity, de-trapping time, and trap state density. Specifically, large amplitudes and phase lags correspond to high photocarrier density, a result of long local carrier lifetimes; however, for regions associated with mechanical damage or intrinsic material defects, the lower amplitude is generally expected because defects lead to a significant increase of nonradiative recombination rates resulting in a reduction of carrier lifetimes. Comparison between regions 2 and 3

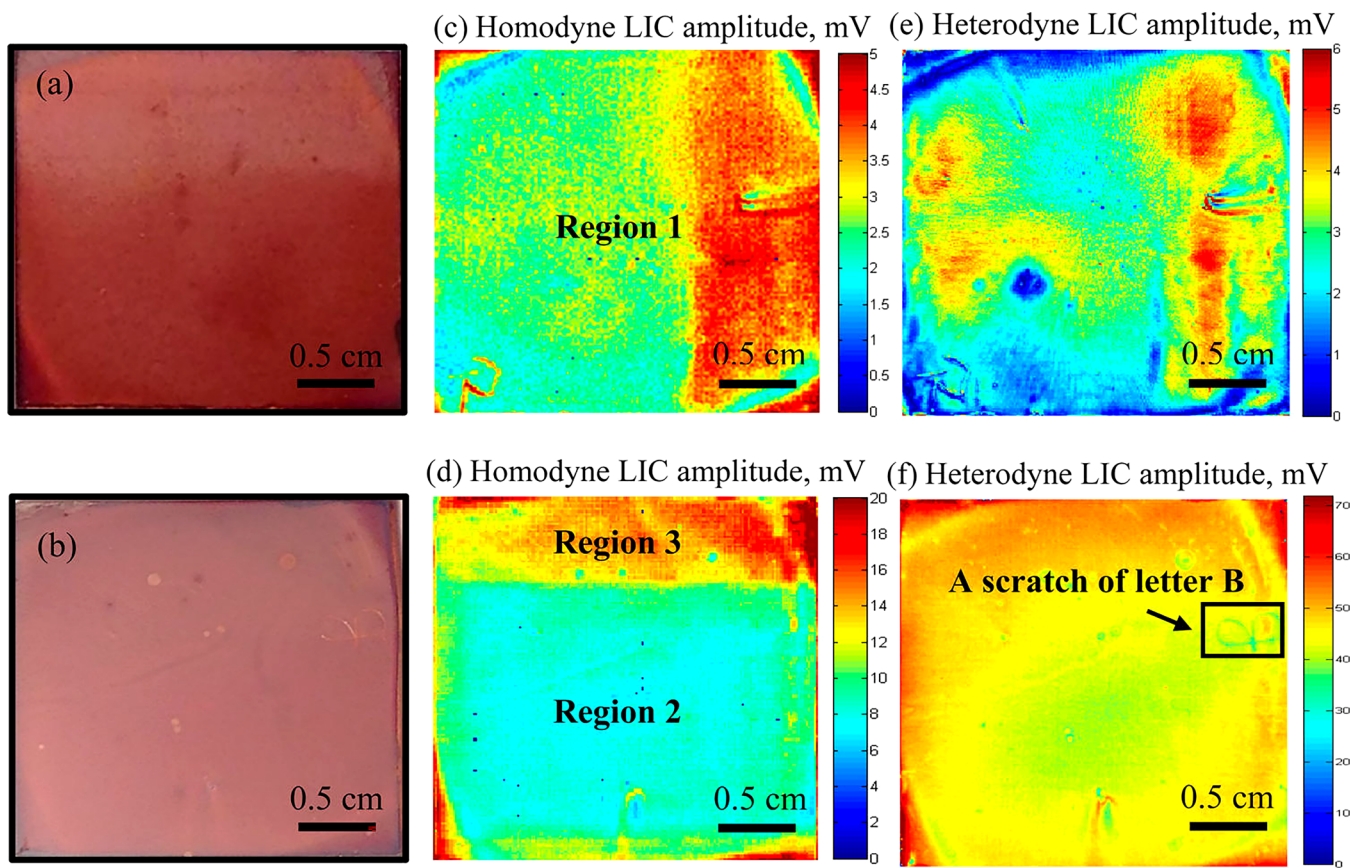


FIG. 27. Photos of MAPbI₃-PbS thin films: (a) sample A and (b) sample B. 1 kHz homodyne LIC amplitude images of MAPbI₃-PbS thin films: (c) sample A and (d) sample B. 20 kHz heterodyne LIC amplitude images of MAPbI₃-PbS thin films: (e) sample A and (f) sample B. Note the very different signal strength scales associated with the two samples. Reproduced with permission from Hu *et al.*, J. Phys. Chem. C **120**(26), 14416–14427 (2016). Copyright 2016 American Physical Society.

in Fig. 27(d) provides a direct example of the LIC image contrast arising from different photocarrier diffusion-wave distributions, with region 3 being indicative of longer carrier lifetimes. This may be due to different spin-coating and ligand passivation processes or unexpected surface chemical reactions upon exposure to ambient air. Regarding mechanical-damage-induced defects, as shown in Fig. 27(f), the area of a scratched letter B on the front surface of sample B exhibits lower PCR amplitude values compared with its neighboring regions. This is attributed to the damage-induced lower photocarrier density diffusion-wave, leading to the enhanced probability of nonradiative recombination into defect states and thus shorter lifetimes. It should be noted that the scratch was produced after the homodyne image of sample B was obtained and shown in Fig. 27(d). For both A and B, homodyne and heterodyne LIC amplitude images show prominent inhomogeneities in the charge carrier density distributions.

III. CONCLUSIONS

CQD solar cells are very promising if they can finally be solution-processed on various substrates, such as window glasses. Although the current power conversion efficiency is as high as 16.5%, this is still insufficient for commercial applications, especially when considering the many engineering issues that researchers are trying to solve nowadays. Therefore, to improve the performance of CQD solar cells, the understanding of the basic principles behind them and the methodologies to characterize them have been touched on in this tutorial. The measurements of CQD solar cell electrical parameters including carrier lifetime, diffusion length, diffusivity, mobility, drift length, trap state density, and doping density are of great interest. These parameters can be measured using the various characterization techniques as reviewed here: SCVD/OCVD, PCD, dc PL, and time-resolved TRPL, PTR, PCR, and HoLIC/HeLIC. As photovoltaic characterization techniques are moving from contact to non-contact, from steady-state to dynamic, and from small-spot testing to large-area imaging, dynamic HeLIC imaging has been developed to obtain the above-mentioned parameters through frequency-scanned imaging. HeLIC overcomes the limitations of low frame rate and long exposure time even for state-of-the-art NIR cameras. HeLIC has achieved ultrahigh-frequency (~ 270 kHz) imaging of CQD solar cells through heterodyne principles and excess carrier-diffusion-wave modeling. High-frequency images lead to carrier transport parameter imaging, which is essential for CQD solar cell optoelectronic homogeneity and quality assessment, fundamental physical carrier transport studies, and a deeper understanding of the role of CQD/contact interfaces in limiting solar efficiency.

ACKNOWLEDGMENTS

The authors acknowledge the Natural Sciences and Engineering Research Council of Canada (NSERC) for a Discovery grant to A.M. and the Canada Research Chairs program.

DATA AVAILABILITY

The data that support the findings of this study are available within the article.

REFERENCES

- ¹M. Hao, Y. Bai, S. Zeiske, L. Ren, J. Liu, Y. Yuan, N. Zarabi, N. Cheng, M. Ghasemi, P. Chen, M. Lyu *et al.*, “Ligand-assisted cation-exchange engineering for high-efficiency colloidal $\text{Cs}_{1-x}\text{FA}_x\text{PbI}_3$ quantum dot solar cells with reduced phase segregation,” *Nat. Energy* **5**(1), 79–88 (2020).
- ²K. Kawaguchi, M. Ekawa, A. Kuramata, T. Akiyama, H. Ebe, M. Sugawara, and Y. Arakawa, “Fabrication of InAs quantum dots on InP (100) by metalorganic vapor-phase epitaxy for 1.55 μm optical device applications,” *Appl. Phys. Lett.* **85**(19), 4331–4333 (2004).
- ³A. Krier, Z. Labadi, and A. Hammiche, “InAsSbP quantum dots grown by liquid phase epitaxy,” *J. Phys. D* **32**(20), 2587 (1999).
- ⁴S. Franchi, G. Trevisi, L. Seravalli, and P. Frigeri, “Quantum dot nanostructures and molecular beam epitaxy,” *Prog. Cryst. Growth Charact. Mater.* **47**(2–3), 166–195 (2003).
- ⁵X. Wang, J. Zhuang, Q. Peng, and Y. Li, “A general strategy for nanocrystal synthesis,” *Nature* **437**(7055), 121 (2005).
- ⁶C. B. Murray, C. R. Kagan, and M. G. Bawendi, “Synthesis and characterization of monodisperse nanocrystals and close-packed nanocrystal assemblies,” *Annu. Rev. Mater. Sci.* **30**(1), 545–610 (2000).
- ⁷C. R. Kagan and C. B. Murray, “Charge transport in strongly coupled quantum dot solids,” *Nat. Nanotechnol.* **10**(12), 1013 (2015).
- ⁸X. Lan, O. Voznyy, A. Kiani, F. P. García de Arquer, A. S. Abbas, G. H. Kim, M. Liu, Z. Yang, G. Walters, J. Xu, M. Yuan *et al.*, “Passivation using molecular halides increases quantum dot solar cell performance,” *Adv. Mater.* **28**(2), 299–304 (2016).
- ⁹M. Liu, O. Voznyy, R. Sabatini, F. P. G. D. Arquer, R. Munir, A. H. Balawi, X. Lan, F. Fan, G. Walters, A. R. Kirmani, S. Hoogland *et al.*, “Hybrid organic-inorganic inks flatten the energy landscape in colloidal quantum dot solids,” *Nat. Mater.* **16**, 258–263 (2017).
- ¹⁰L. Hu, A. Mandelis, Z. Yang, X. Guo, X. Lan, M. Liu, G. Walters, A. Melnikov, and E. H. Sargent, “Temperature-and ligand-dependent carrier transport dynamics in photovoltaic PbS colloidal quantum dot thin films using diffusion-wave methods,” *Sol. Energy Mater. Sol. Cells* **164**, 135–145 (2017).
- ¹¹R. A. Marcus, “Chemical and electrochemical electron-transfer theory,” *Annu. Rev. Phys. Chem.* **15**(1), 155–196 (1964).
- ¹²C. A. Leatherdale, C. R. Kagan, N. Y. Morgan, S. A. Empedocles, M. A. Kastner, and M. G. Bawendi, “Photoconductivity in CdSe quantum dot solids,” *Phys. Rev. B* **62**(4), 2669 (2000).
- ¹³A. Mandelis, L. Hu, and J. Wang, “Quantitative measurements of charge carrier hopping transport properties in depleted-heterojunction PbS colloidal quantum dot solar cells from temperature dependent current–voltage characteristics,” *RSC Adv.* **6**(95), 93180–93194 (2016).
- ¹⁴L. Brus, “Model for carrier dynamics and photoluminescence quenching in wet and dry porous silicon thin films,” *Phys. Rev. B* **53**(8), 4649 (1996).
- ¹⁵I. H. Chu, M. Radulaski, N. Vukmirovic, H. Cheng, and L. Wang, “Charge transport in a quantum dot supercrystal,” *J. Phys. Chem. C* **115**(43), 21409–21415 (2011).
- ¹⁶H. E. Romero and M. Drndic, “Coulomb blockade and hopping conduction in PbSe quantum dots,” *Phys. Rev. Lett.* **95**(15), 156801 (2005).
- ¹⁷S. Xu, D. Thian, S. Wang, Y. Wang, and F. B. Prinz, “Effects of size polydispersity on electron mobility in a two-dimensional quantum-dot superlattice,” *Phys. Rev. B* **90**(14), 144202 (2014).
- ¹⁸Y. Liu, M. Gibbs, J. Puthussery, S. Gaik, R. Ihly, H. W. Hillhouse, and M. Law, “Dependence of carrier mobility on nanocrystal size and ligand length in PbSe nanocrystal solids,” *Nano Lett.* **10**(5), 1960–1969 (2010).
- ¹⁹M. S. Kang, A. Sahu, D. J. Norris, and C. D. Frisbie, “Size-and temperature-dependent charge transport in PbSe nanocrystal thin films,” *Nano Lett.* **11**(9), 3887–3892 (2011).
- ²⁰M. S. Kang, A. Sahu, D. J. Norris, and C. D. Frisbie, “Size-dependent electrical transport in CdSe nanocrystal thin films,” *Nano Lett.* **10**(9), 3727–3732 (2010).
- ²¹J. Wang, A. Mandelis, A. Melnikov, S. Hoogland, and E. H. Sargent, “Exciton lifetime broadening and distribution profiles of PbS colloidal quantum dot thin

- films using frequency-and temperature-scanned photocarrier radiometry," *J. Phys. Chem. C* **117**(44), 23333–23348 (2013).
- ²²J. Wang and A. Mandelis, "Variational reconstruction of exciton multipath deexcitation lifetime spectra in coupled PbS colloidal quantum dots," *J. Phys. Chem. C* **118**(33), 19484–19491 (2014).
- ²³N. Kholmicheva, P. Moroz, E. Bastola, N. Razgoniaeva, J. Bocanegra, M. Shaughnessy, Z. Porach, D. Khon, and M. Zamkov, "Mapping the exciton diffusion in semiconductor nanocrystal solids," *ACS Nano* **9**(3), 2926–2937 (2015).
- ²⁴J. Gao, J. Zhang, J. Lagemaat, J. C. Johnson, and M. C. Beard, "Charge generation in PbS quantum dot solar cells characterized by temperature-dependent steady-state photoluminescence," *ACS Nano* **8**(12), 12814–12825 (2014).
- ²⁵J. Tang and E. H. Sargent, "Infrared colloidal quantum dots for photovoltaics: Fundamentals and recent progress," *Adv. Mater.* **23**, 12–29 (2011).
- ²⁶J. Lee, O. Choi, and E. Sim, "Nonmonotonic size-dependent carrier mobility in PbSe nanocrystal arrays," *J. Phys. Chem. Lett.* **3**(6), 714–719 (2012).
- ²⁷D. Zhitomirsky, I. J. Kramer, A. J. Labelle, A. Fischer, R. Debnath, J. Pan, O. M. Bakr, and E. H. Sargent, "Colloidal quantum dot photovoltaics: The effect of polydispersity," *Nano Lett.* **12**(2), 1007–1012 (2012).
- ²⁸M. Liu, F. P. G. de Arquer, Y. Li, X. Lan, G. H. Kim, O. Voznyy, L. K. Jagadamma, A. S. Abbas, S. Hoogland, Z. Lu, and J. Y. Kim, "Double-sided junctions enable high-performance colloidal-quantum-dot photovoltaics," *Adv. Mater.* **28**(21), 4142–4148 (2016).
- ²⁹C. H. M. Chuang, A. Maurano, R. E. Brandt, G. W. Hwang, J. Jean, T. Buonassisi, V. Bulovic, and M. G. Bawendi, "Open-circuit voltage deficit, radiative sub-bandgap states, and prospects in quantum dot solar cells," *Nano Lett.* **15**(5), 3286–3294 (2015).
- ³⁰B. Sun, O. Voznyy, H. Tan, P. Stadler, M. Liu, G. Walters, A. H. Proppe, M. Liu, J. Fan, T. Zhuang, and J. Li, "Pseudohalide-exchanged quantum dot solids achieve record quantum efficiency in infrared photovoltaics," *Adv. Mater.* **29**(27), 1700749 (2017).
- ³¹N. Kholmicheva, P. Moroz, H. Eckard, G. Jensen, and M. Zamkov, "Energy transfer in quantum dot solids," *ACS Energy Lett.* **2**(1), 154–160 (2017).
- ³²M. Liu, F. Che, B. Sun, O. Voznyy, A. Proppe, R. Munir, M. Wei, R. Quintero-Bermudez, L. Hu, S. Hoogland, A. Mandelis *et al.*, "Controlled steric hindrance enables efficient ligand exchange for stable, infrared-bandgap quantum dot inks," *ACS Energy Lett.* **4**(6), 1225–1230 (2019).
- ³³See <https://www.nrel.gov/pv/assets/pdfs/best-research-cell-efficiencies.20200925.pdf> state-of-the-art research on solar cell efficiencies (last accessed November 26, 2020).
- ³⁴R. D. Schaller and V. I. Klimov, "High efficiency carrier multiplication in PbSe nanocrystals: Implications for solar energy conversion," *Phys. Rev. Lett.* **92**(18), 186601 (2004).
- ³⁵A. J. Nozik, "Quantum dot solar cells," *Phys. E* **14**, 115–120 (2002).
- ³⁶A. J. Nozik, "Multiple exciton generation in semiconductor quantum dots," *Chem. Phys. Lett.* **457**, 3–11 (2008).
- ³⁷M. C. Hanna and A. J. Nozik, "Solar conversion efficiency of photovoltaic and photoelectrolysis cells with carrier multiplication absorbers," *J. Appl. Phys.* **100**, 074510 (2006).
- ³⁸A. G. Pattantyus-Abrraham, I. J. Kramer, A. R. Barkhouse, X. Wang, G. Konstantatos, R. Debnath, L. Levina, I. Raabe, M. K. Nazeeruddin, M. Grätzel, and E. H. Sargent, "Depleted-heterojunction colloidal quantum dot solar cells," *ACS Nano* **4**(6), 3374–3380 (2010).
- ³⁹J. Jean, S. Chang, P. R. Brown, J. J. Cheng, P. H. Rekemeyer, M. G. Bawendi, S. Gradečák, and V. Bulović, "ZnO nanowire arrays for enhanced photocurrent in PbS quantum dot solar cells," *Adv. Mater.* **25**, 2790–2796 (2013).
- ⁴⁰G. H. Carey, A. L. Abdelhady, Z. Ning, S. M. Thon, O. M. Bakr, and E. H. Sargent, "Colloidal quantum dot solar cells," *Chem. Rev.* **115**, 12732–12763 (2015).
- ⁴¹I. J. Kramer, D. Zhitomirsky, J. D. Bass, P. M. Rice, T. Topuria, L. Krupp, S. M. Thon, A. H. Ip, R. Debnath, H. C. Kim, and E. H. Sargent, "Ordered nanopillar structured electrodes for depleted bulk heterojunction colloidal quantum dot solar cells," *Adv. Mater.* **24**, 2315–2319 (2012).
- ⁴²H. Wang, T. Kubo, J. Nakazaki, T. Kinoshita, and H. Segawa, "PbS-quantum-dot-based heterojunction solar cells utilizing ZnO nanowires for high external quantum efficiency in the near-infrared region," *J. Phys. Chem. Lett.* **4**, 2455–2460 (2013).
- ⁴³J. Chang, Y. Kuga, I. Mora-Seró, T. Toyoda, Y. Ogomi, S. Hayase, J. Bisquert, and Q. Shen, "High reduction of interfacial charge recombination in colloidal quantum dot solar cells by metal oxide surface passivation," *Nanoscale* **7**, 5446–5456 (2015).
- ⁴⁴H. Wang, T. Kubo, J. Nakazaki, and H. Segawa, "PbS colloidal quantum dot/ZnO-based bulk-heterojunction solar cells with high stability under continuous light soaking," *Phys. Status Solidi RRL* **8**, 961–965 (2014).
- ⁴⁵H. Wang, V. Gonzalez-Pedro, T. Kubo, F. Fabregat-Santiago, J. Bisquert, Y. Sanehira, J. Nakazaki, and H. Segawa, "Enhanced carrier transport distance in colloidal PbS quantum-dot-based solar cells using ZnO nanowires," *J. Phys. Chem. C* **119**, 27265–27274 (2015).
- ⁴⁶T. Kawakami, H. Wang, T. Kubo, K. Saito, J. Nakazaki, H. Segawa, and T. Tatsuma, "Efficiency enhancement of PbS quantum dot/ZnO nanowire bulk heterojunction solar cells by plasmonic silver nanocubes," *ACS Nano* **9**, 4165–4172 (2015).
- ⁴⁷K. S. Leschkies, T. J. Beatty, M. S. Kang, D. J. Norris, and E. S. Aydil, "Solar cells based on junctions between colloidal PbSe nanocrystals and thin ZnO films," *ACS Nano* **3**, 3638–3648 (2009).
- ⁴⁸U. Würfel, D. Neher, A. Spies, and S. Albrecht, "Impact of charge transport on current-voltage characteristics and power-conversion efficiency of organic solar cells," *Nat. Commun.* **6**, 6951 (2015).
- ⁴⁹L. Hu, M. Liu, A. Mandelis, A. Melnikov, and E. H. Sargent, "Colloidal quantum dot solar cell power conversion efficiency optimization using analysis of current-voltage characteristics and electrode contact imaging by lock-in carriography," *Progr. Photovolt.* **25**(12), 1034–1050 (2017).
- ⁵⁰A. Le Bris and J. F. Guillemoles, "Hot carrier solar cells achievable efficiency accounting for heat losses in the absorber and through contacts," *Appl. Phys. Lett.* **97**, 113506 (2010).
- ⁵¹A. Pandey and P. Guyot-Sionnest, "Slow electron cooling in colloidal quantum dots," *Science* **322**(5903), 929–932 (2008).
- ⁵²A. Pandey and P. Guyot-Sionnest, "Hot electron extraction from colloidal quantum dots," *J. Phys. Chem. Lett.* **1**(1), 45–47 (2009).
- ⁵³W. A. Tisdale, K. J. Williams, B. A. Timp, D. J. Norris, E. S. Aydil, and X. Y. Zhu, "Hot-electron transfer from semiconductor nanocrystals," *Science* **328**(5985), 1543–1547 (2010).
- ⁵⁴V. Sukhovatkin, S. Hinds, L. Brzozowski, and E. H. Sargent, "Colloidal quantum-dot photodetectors exploiting multiexciton generation," *Science* **324**(5934), 1542–1544 (2009).
- ⁵⁵J. E. Murphy, M. C. Beard, A. G. Norman, S. P. Ahrenkiel, J. C. Johnson, P. Yu, O. I. Mićić, R. J. Ellingson, and A. J. Nozik, "PbTe colloidal nanocrystals: Synthesis, characterization, and multiple exciton generation," *J. Am. Chem. Soc.* **128**(10), 3241–3247 (2006).
- ⁵⁶M. C. Beard, K. P. Knutsen, P. Yu, J. M. Luther, Q. Song, W. K. Metzger, R. J. Ellingson, and A. J. Nozik, "Multiple exciton generation in colloidal silicon nanocrystals," *Nano Lett.* **7**(8), 2506–2512 (2007).
- ⁵⁷Y. Ryan, R. W. Crisp, J. Gu, B. D. Chernomordik, G. F. Pach, A. R. Marshall, J. A. Turner, and M. C. Beard, "Multiple exciton generation for photoelectrochemical hydrogen evolution reactions with quantum yields exceeding 100%," *Nat. Energy* **2**, 17052 (2017).
- ⁵⁸M. T. Trinh, A. J. Houtepen, J. M. Schins, T. Hanrath, J. Piris, W. Knulst, A. P. Goossens, and L. D. Siebbeles, "In spite of recent doubts carrier multiplication does occur in PbSe nanocrystals," *Nano Lett.* **8**(6), 1713–1718 (2008).
- ⁵⁹R. D. Schaller, M. Sykora, S. Jeong, and V. I. Klimov, "High-efficiency carrier multiplication and ultrafast charge separation in semiconductor nanocrystals studied via time-resolved photoluminescence," *J. Phys. Chem. B* **110**(50), 25332–25338 (2006).
- ⁶⁰R. D. Schaller, M. A. Petruska, and V. I. Klimov, "Effect of electronic structure on carrier multiplication efficiency: Comparative study of PbSe and CdSe nanocrystals," *Appl. Phys. Lett.* **87**(25), 253102 (2005).
- ⁶¹J. J. H. Pijpers, E. Hendry, M. T. W. Milder, R. Fanciulli, J. Savolainen, J. L. Herek, D. Vanmaekelbergh, S. Ruhman, D. Mocatta, D. Oron, A. Aharoni,

- U. Banin, and M. Bonn, "Carrier multiplication and its reduction by photodoping in colloidal InAs quantum dots," *J. Phys. Chem. C* **111**(11), 4146–4152 (2007).
- ⁶²S. K. Stubbs, S. J. Hardman, D. M. Graham, B. F. Spencer, W. R. Flavell, P. Glarvey, O. Masala, N. L. Pickett, and D. J. Binks, "Efficient carrier multiplication in InP nanoparticles," *Phys. Rev. B* **81**(8), 081303 (2010).
- ⁶³Y. Kobayashi, T. Udagawa, and N. Tamai, "Carrier multiplication in CdTe quantum dots by single-photon timing spectroscopy," *Chem. Lett.* **38**(8), 830–831 (2009).
- ⁶⁴J. Gao, J. M. Luther, O. E. Semenin, R. J. Ellingson, A. J. Nozik, and M. C. Beard, "Quantum dot size dependent J-V characteristics in heterojunction ZnO/PbS quantum dot solar cells," *Nano Lett.* **11**, 1002–1008 (2011).
- ⁶⁵J. Tang, K. W. Kemp, S. Hoogland, K. S. Jeong, H. Liu, L. Levina, M. Furukawa, X. Wang, R. Debnath, D. Cha, K. W. Chou, *et al.*, "Colloidal-quantum-dot photovoltaics using atomic-ligand passivation," *Nat. Mater.* **10**, 765–771 (2011).
- ⁶⁶A. H. Ip, S. M. Thon, S. Hoogland, O. Voznyy, D. Zhitomirsky, R. Debnath, L. Levina, L. R. Rollny, G. H. Carey, A. Fischer, K. W. Kemp *et al.*, "Hybrid passivated colloidal quantum dot solids," *Nat. Nanotechnol.* **7**, 577–582 (2012).
- ⁶⁷C. H. M. Chuang, P. R. Brown, V. Bulović, and M. G. Bawendi, "Improved performance and stability in quantum dot solar cells through band alignment engineering," *Nat. Mater.* **13**(8), 796 (2014).
- ⁶⁸G. H. Kim, F. P. García de Arquer, Y. J. Yoon, X. Lan, M. Liu, O. Voznyy, L. Krishnan Jagadamma, A. Saud Abbas, Z. Yang, F. Fan, A. H. Ip *et al.*, "Correction to high-efficiency colloidal quantum dot photovoltaics via robust self-assembled monolayers," *Nano Lett.* **16**, 822 (2016).
- ⁶⁹K. W. Johnston, A. G. Pattantyus-Abraham, J. P. Clifford, S. H. Myrskog, S. Hoogland, H. Shukla, E. J. Klem, L. Levina, and E. H. Sargent, "Efficient Schottky-quantum-dot photovoltaics: The roles of depletion, drift, and diffusion," *Appl. Phys. Lett.* **92**(12), 122111 (2008).
- ⁷⁰J. E. Mahan, T. W. Ekstedt, R. I. Frank, and R. Kaplow, "Measurement of minority carrier lifetime in solar cells from photo-induced open circuit voltage decay," *IEEE Trans. Electron Dev.* **26**, 733–739 (1979).
- ⁷¹B. H. Rose and H. T. Weaver, "Determination of effective surface recombination velocity and minority-carrier lifetime in high-efficiency Si solar cells," *J. Appl. Phys.* **54**, 238–247 (1983). Corrections, *J. Appl. Phys.* **55**, 607 (1984).
- ⁷²R. J. Bassett, W. Eulop, and C. A. Hogarth, "Determination of the bulk carrier lifetime in the low-doped region of a silicon power diode, by the method of open circuit voltage decay," *Int. J. Electr.* **35**(2), 177–192 (1973).
- ⁷³A. Sanders and M. Kunst, "Characterization of silicon wafers by transient microwave photoconductivity measurements," *Solid-State Electron.* **34**, 1007–1015 (1991).
- ⁷⁴E. Gaubas and A. Kaniava, "Determination of recombination parameters in silicon wafers by transient microwave absorption," *Rev. Sci. Instrum.* **67**, 2339–2345 (1996).
- ⁷⁵S. M. Sze, *Physics of Semiconductor Devices* (John Wiley & Sons, New York, NY, 1981).
- ⁷⁶R. W. Crisp, N. Kirkwood, G. Grimaldi, S. Kinge, L. D. Siebbeles, and A. J. Houtepen, "Highly photoconductive InP quantum dots films and solar cells," *ACS Appl. Energy Mater.* **1**(11), 6569–6576 (2018).
- ⁷⁷L. Hu, Z. Yang, A. Mandelis, A. Melnikov, X. Lan, G. Walters, S. Hoogland, and E. H. Sargent, "Quantitative analysis of trap-state-mediated exciton transport in perovskite shelled PbS quantum dot thin films using photocarrier diffusion-wave nondestructive evaluation and imaging," *J. Phys. Chem. C* **120**(26), 14416–14427 (2016).
- ⁷⁸K. L. Luke and L. Cheng, "Analysis of the interaction of a laser pulse with a silicon wafer: Determination of bulk lifetime and surface recombination velocity," *J. Appl. Phys.* **61**(6), 2282–2293 (1987).
- ⁷⁹K. Wang, W. McLean, and H. Kampwerth, "Transient photoluminescence from silicon wafers: Finite element analysis," *J. Appl. Phys.* **114**(16), 163105 (2013).
- ⁸⁰R. K. Ahrenkiel, "Measurement of minority-carrier lifetime by time-resolved photoluminescence," *Solid-State Electron.* **35**, 239–250 (1992).
- ⁸¹A. P. Litvin, E. V. Ushakova, P. S. Parfenov, A. V. Fedorov, and A. V. Baranov, "FRET between close-packed quasi-monodispersed PbS QDs in a porous matrix," *J. Phys. Chem. C* **118**(12), 6531–6535 (2014).
- ⁸²L. Hu, A. Mandelis, A. Melnikov, X. Lan, S. Hoogland, and E. H. Sargent, "Study of exciton hopping transport in PbS colloidal quantum dot thin films using frequency-and temperature-scanned photocarrier radiometry," *Int. J. Thermophys.* **38**(1), 7 (2017).
- ⁸³L. Hu, M. Liu, A. Mandelis, Q. Sun, A. Melnikov, and E. H. Sargent, "Colloidal quantum dot solar cell electrical parameter non-destructive quantitative imaging using high-frequency heterodyne lock-in carrierography and photocarrier radiometry," *Sol. Energy Mater. Sol. Cells* **174**, 405–411 (2018).
- ⁸⁴J. A. Giesecke, B. Michl, F. Schindler, M. C. Schubert, and W. Warta, "Minority carrier lifetime of silicon solar cells from quasi-steady-state photoluminescence," *Sol. Energy Mater. Sol. Cells* **95**(7), 1979–1982 (2011).
- ⁸⁵A. Mandelis, J. Batista, and D. Shaughnessy, "Infrared photocarrier radiometry of semiconductors: Physical principles, quantitative depth profilometry, and scanning imaging of deep subsurface electronic defects," *Phys. Rev. B* **67**(20), 205208 (2003).
- ⁸⁶A. Salnick, A. Mandelis, and C. Jean, "Noncontact measurement of transport properties of long-bulk-carrier-lifetime Si wafers using photothermal radiometry," *Appl. Phys. Lett.* **69**(17), 2522–2524 (1996).
- ⁸⁷A. Salnick, A. Mandelis, and C. Jean, "Infrared photothermal radiometric deep-level transient spectroscopy of shallow B⁺ dopant states in p-Si," *Appl. Phys. Lett.* **71**(18), 2671–2673 (1997).
- ⁸⁸K. Ramspeck, K. Bothe, J. Schmidt, and R. Brendel, "Combined dynamic and steady-state infrared camera based carrier lifetime imaging of silicon wafers," *J. Appl. Phys.* **106**(11), 114506 (2009).
- ⁸⁹D. Kiliani, G. Micard, B. Steuer, B. Raabe, A. Herguth, and G. Hahn, "Minority charge carrier lifetime mapping of crystalline silicon wafers by time-resolved photoluminescence imaging," *J. Appl. Phys.* **110**(5), 054508 (2011).
- ⁹⁰T. Ikari, A. Salnick, and A. Mandelis, "Theoretical and experimental aspects of three-dimensional infrared photothermal radiometry of semiconductors," *J. Appl. Phys.* **85**(10), 7392–7397 (1999).
- ⁹¹A. Rosencwaig and A. Gersho, "Theory of the photoacoustic effect with solids," *J. Appl. Phys.* **47**(1), 64–69 (1976).
- ⁹²J. Xia and A. Mandelis, "Broadening effects and ergodicity in deep level photothermal spectroscopy of defect states in semi-insulating GaAs: A combined temperature-, pulse-rate-, and time-domain study of defect state kinetics," *J. Appl. Phys.* **105**(10), 103712 (2009).
- ⁹³S. Rein, *Lifetime Spectroscopy: A Method of Defect Characterization in Silicon for Photovoltaic Applications* (Springer, Berlin, 2005).
- ⁹⁴P. Würfel, *Physics of Solar Cells: From Basic Principles to Advanced Concepts* (Wiley-VCH, Weinheim, 2009).
- ⁹⁵A. Richter, S. W. Glunz, F. Werner, J. Schmidt, and A. Cuevas, "Improved quantitative description of Auger recombination in crystalline silicon," *Phys. Rev. B* **86**, 165202 (2012).
- ⁹⁶L. Hu, A. Mandelis, and Q. Sun, "Ultrahigh-Frequency heterodyne lock-in carrierography for large-scale quantitative multi-parameter imaging of colloidal quantum dot solar cells," *IEEE J. Photovoltaics* **9**(1), 132–138 (2018).
- ⁹⁷Q. Sun, A. Melnikov, and A. Mandelis, "Camera-based high frequency heterodyne lock-in carrierographic (frequency-domain photoluminescence) imaging of crystalline silicon wafers," *Phys. Status Solidi (A)* **213**(2), 405–411 (2016).
- ⁹⁸See https://en.wikipedia.org/wiki/Nyquist%20%93Shannon_sampling_theorem for information about the Nyquist–Shannon sampling theorem.
- ⁹⁹United States Bureau of Naval Personnel, *Basic Electronics* (USA Courier Dover, 1973), p. 338.